

# Combining spectroscopic and photometric surveys using angular cross-correlations II: Parameter constraints from different physical effects

Martin Eriksen<sup>1,2</sup>, Enrique Gaztañaga<sup>1</sup>

<sup>1</sup>*Institut de Ciències de l'Espai (IEEC-CSIC), E-08193 Bellaterra (Barcelona), Spain*

<sup>2</sup>*Leiden Observatory, Leiden University, PO Box 9513, NL-2300 RA Leiden, Netherlands*

6 September 2021

## ABSTRACT

Future spectroscopic and photometric surveys will measure accurate positions and shapes of an increasing number of galaxies. In the previous paper of this series we studied the effects of Redshift Space Distortions (RSD), baryon acoustic oscillations (BAO) and Weak gravitational Lensing (WL) using angular cross-correlation. Here, we provide a new forecast that explores the contribution of including different observables, physical effects (galaxy bias, WL, RSD, BAO) and approximations (non-linearities, Limber approximation, covariance between probes). The radial information is included by using the cross-correlation of separate narrow redshift bins. For the auto correlation the separation of galaxy pairs is mostly transverse, while the cross-correlations also includes a radial component. We study how this information adds to our figure of merit (FoM), which includes the dark energy equation of state  $w(z)$  and the growth history, parameterized by  $\gamma$ . We show that the Limber approximation and galaxy bias are the most critical ingredients to the modelling of correlations. Adding WL increases our FoM by 4.8, RSD by 2.1 and BAO by 1.3. We also explore how overlapping surveys perform under the different assumption and for different figures of merit. Our qualitative conclusions depend on the survey choices and scales included, but we find some clear tendencies that highlight the importance of combining different probes and can be used to guide and optimise survey strategies.

## 1 INTRODUCTION

The expansion of the universe provide a challenge for cosmology and fundamental physics. Understanding the recent accelerated expansion of the universe is connected to dark matter and dark energy, either by determining their properties or by providing an alternative theory. There is no scarcity of models, but no model beyond  $\Lambda$ CDM has emerged as a natural candidate to explain the cosmic acceleration.

Galaxy surveys are designed to probe cosmology in different manners. Weak lensing of foreground matter affects the galaxy shapes. Observing the weak lensing through galaxy shapes (shear) (Massey et al. 2007; Schrabback et al. 2010) requires deep imaging surveys like DES and the upcoming Euclid and LSST. Further, overdensities of dark matter attracts nearby galaxies, which creates an additional peculiar velocity. The radial component of the extra velocity results in a shift in redshift, which is the effect of redshift space distortions (RSD). Optimal measurement of RSD require accurate redshift and the method is most suitable for spectroscopic surveys.

The lensing efficiency has a broad kernel and the shear-

shear lensing signal can be analyzed in 5-10 broad redshift bins. The RSD signal is traditionally analyzed using power spectrum analysis in 3D comoving space, which includes a cosmology dependent conversion transformation of angles and redshift to the 3D comoving distances. As shown in paper-I (and references therein), angular correlations can also be used to measure RSD. A previous study Asorey et al. (2012) found that angular correlations in narrow redshift bins can recover most of the information in the 3D power spectrum. In these papers we use the angular correlation for both the photometric (WL) and spectroscopic (RSD, WL) survey.

Using a single set of observables for WL and RSD has several advantages. For overlapping surveys the galaxies trace the same matter fluctuations, which introduce a covariance between the surveys. Particular care is needed to not double counting information when jointly observing shear-shear in the lensing survey, the 3D power spectrum for the spectroscopic survey and 2D correlations for the counts-shear cross-correlations between the two. For example counting the modes is insufficient if including photo- $z$  effects in the 3D sample since the photo- $z$  affects the radial and transverse modes differently.

Several groups have explored combining weak lensing and spectroscopic surveys (Bernstein & Cai 2011; Gaztañaga et al. 2012; Cai & Bernstein 2012; Kirk et al. 2013; Font-Ribera et al. 2013; de Putter, Doré & Takada 2013). In overlapping surveys (same-sky) one can cross-correlate the observables, e.g. galaxy counts from the two surveys or galaxy counts from the spectroscopic sample with background shear from the lensing survey. Overlapping samples further reduce the sample variance (McDonald & Seljak 2009). While non-overlapping surveys benefits from larger area, several authors find stronger parameter constraints when combining weak lensing and spectroscopic surveys over the same area. In this paper we study the importance of different physical effects for overlapping and non-overlapping surveys, while the paper Eriksen & Gaztanaga (2014a) elaborate on the benefit of overlapping surveys.

Galaxies are theoretically (Scoccimarro et al. 2001) and observationally expected to form in overdense regions. Unlike shear which is affected by all foreground matter, the galaxy counts relates to the underlying matter distribution at a given redshift. The negative aspect of probing cosmology with the galaxy counts is requiring to understand and marginalise over uncertainties in the relation between matter and galaxy overdensities, the galaxy bias (Gaztañaga et al. 2012). One can either approach the galaxy bias by only using the BAO peak (Seo & Eisenstein 2003, 2007) or parameterize the bias (Shoji, Jeong & Komatsu 2009). In this paper we use the full galaxy correlation and measure the bias parameters by combining LSS and lensing in a multiple tracer analysis.

Magnification change the overdensities of number counts through two weak lensing effects. In a magnitude limited sample, lensed galaxies appear brighter and enters into the sample when magnified over the magnitude cut. The magnification also magnifies the area which reduces the number density. In the SDSS sample magnification has been observed by correlating foreground galaxies with background quasars (Scranton et al. 2005; Ménard et al. 2010). While the shear-shear signal has less noise, magnification provides an additional signal which is already present in the galaxy catalogs. This paper, in a similar way to Gaztañaga et al. (2012); Duncan et al. (2014), will study the benefits of magnification when combining the analysis of spectroscopic and photometric surveys in angular correlations.

Photometric surveys conventionally use broad band filters. Two upcoming surveys, PAU<sup>1</sup> and J-PAS<sup>2</sup> plan to measure photometry for galaxies in 40 to 50 narrow (100-130Å) bands. For PAU the resulting photo-z precision is  $\sigma_{68} \approx 0.0035(1+z)$  for  $i_{AB} \leq 22.5$  (Martí et al. 2014). In addition the PAUcam broad bands (ugrizY) has an anticipated photo-z accuracy of  $\sigma_{68} = 0.05(1+z)$  for  $22.5 < i_{AB} < 24.1$ . The PAU survey at the William Herschel Telescope (WHT) can cover about 200 sq.deg. to  $i_{AB} < 22.5$  in narrow bands and  $i_{AB} < 24$  with broad bands in 100 nights. These defines two magnitude limited populations of Bright (B) galaxies ( $i_{AB} < 22.5$ ) and Faint (F) galaxies ( $22.5 < i_{AB} < 24$ ) similar to two overlapping spectroscopic and photometric surveys.

This paper (paper-II) is part of a three paper series. The first paper (paper-I, Eriksen & Gaztanaga (2014b)) dealt with modelling of the correlation function, focusing in particular on the effect of RSD, BAO and the Limber approximation in narrow bins. Here (paper-II) we forecast the relative impact of WL, RSD and BAO in upcoming cosmological surveys. A third paper (paper-III, Eriksen & Gaztanaga (2015)) study the impact of galaxy bias, while a separate paper (Eriksen & Gaztanaga 2014a) focus on the benefit of overlapping surveys.

This paper is organised in the following manner. The second section present the assumptions, which includes Fisher matrix formalism, forecast assumptions and nomenclature. In the third section we compare the relative contribution of the different effect (including WL, RSD, BAO, magnification) and the Limber approximation. Last section is the conclusion.

## 2 FORECAST ASSUMPTIONS

This section first present the assumptions fiducial cosmology, galaxy bias parameterization, galaxy samples, surveys definitions, cuts in non-linear scales and the Fisher forecast. Paper-I included the theoretical expressions for the  $C_l$  cross-correlations and they are therefore not repeated here. In this section we also define the FoMs and the nomenclature (e.g. FxB, F+B) used throughout the paper.

### 2.1 Fiducial cosmological model.

The cosmological model assumed is  $w$ CDM<sup>3</sup>, which is General Relativity with Cold Dark Matter and a dark energy model with an equation of state  $w \equiv \frac{p_{DE}}{\rho_{DE}}$ . The main observables are  $C_l$  cross-correlations of fluctuations  $\delta(z, k)$ , which depends on the initial power spectrum, distances and the growth of fluctuations. For a Friedmann-Lemaître-Robertson-Walker (FLRW) metric (Dodelson 2003), the Hubble distance is

$$H^2(z) = H_0^2[\Omega_m a^{-3} + \Omega_k a^{-2} + \rho_{DE}(z)] \quad (1)$$

$$\rho_{DE} = \Omega_{DE} a^{-3(1+w_0+w_a)} \exp(-3w_a z/(1+z)) \quad (2)$$

where the last equation expresses the dark energy density using the parameterization

$$w(z) = w_0 + w_a(1-a) \quad (3)$$

from Linder (2003, 2005) for the dark energy equation of state (EoS). Overdensities of matter grow because of gravitational attraction and at large (linear) scales the equation determining the growth has the solutions (Heath 1977; Peebles 1980)

$$\delta(z) = D(z)\delta(0) \quad (4)$$

<sup>3</sup> For the fiducial cosmology we use the values  $\Omega_m = 0.25$ ,  $\Omega_b = 0.044$ ,  $\Omega_{DE} = 0.75$ ,  $h = 0.7$ ,  $w_0 = -1$ ,  $w_a = 0$ ,  $n_s = 0.95$  and  $\sigma_8 = 0.8$ , which correspond to the cosmological model in the MICE (<http://www.ice.cat/mice>) simulation.

<sup>1</sup> [www.pausurvey.org](http://www.pausurvey.org)

<sup>2</sup> [j-pas.org](http://j-pas.org)

where here  $D(z)$  is defined through

$$f \equiv \frac{d \ln(D)}{d \ln(a)} = \frac{\dot{\delta}}{\delta} \equiv \Omega_m^\gamma(a) \quad (5)$$

Normalising the growth to  $D(z=0) = 1$  we have

$$D(z) = \exp \left[ - \int_a^1 d \ln a f(a) \right]. \quad (6)$$

In these papers (and previously in Gaztañaga et al. (2012)) the growth is parameterized through the parameter  $\gamma$  in Eq.5, which is  $\gamma \approx 3/11 \approx 0.55$  in General Relativity with a cosmological constant. For example the DGP model (Dvali, Gabadadze & Porrati 2000) propose to explain the cosmological acceleration through embedding the ordinary 3+1 dimensional Minkowski space in a 4+1 dimensional Minkowski space. Alternatively modified gravity, which we have left of future work, can be parameterized by the Bardeen potentials (Bardeen 1980). Adjusting free parameters in modified gravity can potentially fit the right expansion history (Eq. 2), but it is more difficult to simultaneously fit the expansion and growth history (Eq. 6). Constraining both the growth and expansion history is therefore important to discriminate between different modified gravity models.

## 2.2 Non-linear scales

On larger scales fluctuations are linear. In contrast, for high density regions the structures collapses in a non-linear manner. As a result, predicting the non-linear power spectrum require either simulations (Springel 2005), perturbation theory (Crocco 2007) or fitting functions to simulations (Heitmann et al. 2010, 2009; Lawrence et al. 2010). Here the forecast use the Eisenstein-Hu (Eisenstein & Hu 1998) linear power spectrum. In appendix A we test the effect of including the non-linear contribution.

Even when including non-linear power spectrum contributions, one need to limit the maximum  $k_{max}$  (or minimum  $r_{min}$ ) scale. The Halofit II model is calibrated to 5% percent accuracy for  $k \leq 1h\text{Mpc}^{-1}$  at  $0 \leq z \leq 10$ . Further, we also want to limit observations to scales where the bias (see subsection 2.3) is scale independent. Here and in other papers of these series the maximum scale is defined through

$$\sigma(R_{min}, z) = 1 \quad (7)$$

where  $\sigma(R, z)$  is the fluctuation amplitude smoothed with a Gaussian kernel on a scale  $R$ . From  $k = l/\chi(z)$ , we have

$$k_{max}(z) = \frac{R(0)_{min}}{R(z)_{min}} k_{max}(0) \quad (8)$$

where  $k_{max}(0) = 0.1h^{-1}\text{Mpc}$  is an overall normalisation. In the MICE cosmology and Eisenstein-Hu power spectrum, then

$$k_{max}(z) = \exp(-2.29 + 0.88z) \quad (9)$$

is a good fit for the  $k_{max}$  limit. The conversion to an  $l_{max}$  for which correlations to include is done with

$$k_{max} = \frac{l_{max} + 0.5}{r(z_i)} \quad (10)$$

which uses the scale contributing to LSS and counts-shear correlations in the Limber equation (see paper-I). For cross-correlations we use the minimum  $k_{max}$  from the two redshift bins. The forecast is restricted to  $10 \leq l \leq 300$  and in addition apply the cut above, including for the the shear-shear correlations. To save time, the forecast use  $\Delta l = 10$ . We have tested that the discrete l-values have minimal impact on the forecast.

## 2.3 Galaxy bias

Galaxy overdensities  $\delta$  are in a local bias model (Fry & Gaztanaga 1993) related to matter overdensities  $\delta_m$  through

$$\delta(k, z) = b(z, k) \delta_m(k, z) \quad (11)$$

where the bias  $b(k, z)$  can in general depend on scale and redshift. Each subset of galaxies, of galaxy population, can have different bias since galaxy types (e.g. elliptical and spirals) cluster and evolve differently. When defining populations by magnitude cuts, as we do, the bias also differ because each population contains another mixture of galaxies.

The two galaxy populations (see subsection 2.6) use a different bias and bias nuisance parameters. We use one bias parameter per redshift bin and galaxy population, no scale dependence and no additional bias priors. In addition, the bias can include a stochastic component. A common used measure of non-linearity and the stochasticity is

$$r \equiv \sqrt{\frac{C_{\delta m}}{C_{\delta\delta} C_{\delta m}}} \quad (12)$$

where  $C_{\delta\delta} \equiv \langle \delta\delta \rangle$ ,  $C_{\delta\delta m} \equiv \langle \delta\delta m \rangle$  and  $C_{mm} \equiv \langle \delta_m \delta_m \rangle$  respectively are the counts-counts, counts-matter and matter-matter correlations. For a deterministic and linear bias, then  $r = 1$ . In Gaztañaga et al. (2012) we showed by theoretical models and also simulations that the stochasticity can be treated as a re-normalisation of the bias. Thus we fix the stochasticity to  $r = 1$  and explore the impact of  $r$  in paper-III.

## 2.4 Fisher matrix forecast

The Fisher matrix is a simple and fast method to estimate parameter uncertainties. Deriving the Fisher matrix follow from a Gaussian approximation of the Likelihood expanded around the fiducial value. Sampling the Likelihood with MCMC methods would be more precise, but greatly increase the computation time. Since the Fisher matrix is widely used in the literature, including the results we compare with, we also use the Fisher matrix formalism.

For the correlations  $C_{ij}$  and corresponding covariance  $\text{Cov}$ , the Fisher matrix is

$$F_{\mu\nu} = \sum_{ij,kl} \frac{\partial C_{ij}}{\partial \mu} \text{Cov}^{-1} \frac{\partial C_{kl}}{\partial \nu} \quad (13)$$

where  $\mu$  and  $\nu$  are parameters and the two sums are over

different correlations. If the observable does not enter the forecast, it is not included neither in the sums nor the covariance. One example of dropping observables is the removal of non-linear scales, as explained in the last subsection. The Cramer-Rao bound states that

$$\sigma_\mu^2 \leq F_{\mu\mu}^{-1} \quad (14)$$

where  $F^{-1}$  denote the Fisher matrix inverse and  $\sigma_\mu^2$  the expected parameter variance for the parameter  $\mu$ . The covariance matrix of 2D-correlations when assuming Gaussian fluctuations (Dodelson 2003) is

$$Cov(C_{AB}, C_{DE}) = N^{-1}(l)(C_{AD}C_{BE} + C_{AE}C_{BD}) \quad (15)$$

where number of modes is  $N(l) = 2f_{\text{sky}}(2l+1)/\Delta l$ ,  $f_{\text{sky}}$  is the survey fractional sky coverage and  $\Delta l$  is the band width (bin width in  $l$ ).

Adding constrains from uncorrelated observables require summing up the Fisher matrices. For example the constraints of LSS/WL and CMB is

$$F_{\text{Combined}} = F_{\text{LSS/WL}} + F_{\text{CMB}} \quad (16)$$

when assuming the CMB is sufficiently uncorrelated with the LSS/WL experiment. One can prove Eq.16 using the covariance for two uncorrelated set of parameters is block diagonal and Eq.13 can be split in two parts. For the forecasts all results (unless explicitly stated) add Planck priors<sup>4</sup>.

## 2.5 Figures of Merit (FoMs)

Figure of Merits are a simplified representation of the parameter constraints. A Fisher matrix of  $n$  parameters includes  $n(n+1)/2$  independent entries. Instead of including all the information on the errors and the covariance between parameters present in a covariance matrix, the figure of merit is only a single number. Comparing probes, effects and configurations are greatly simplified when using a single number. The FoMs let us study the gradual change with a parameter given on the x-axis, while adding different lines corresponding to various configurations. Also, the FoM is useful for comparing information along two dimensions in a table. While a single number does not fully capture the utility of a galaxy survey, but is a good measure to discuss trends.

The parameters included in the Fisher matrix forecast are

$$w_0, w_a, h, n_s, \Omega_m, \Omega_b, \Omega_{DE}, \sigma_8, \gamma, \text{Galaxy Bias}$$

where the 9 first parameters equals the one included in the dark energy task force (DETF) figure of merit (Albrecht et al. 2006). The galaxy bias (see subsection 2.3) is parameterized with one parameter in each redshift bin for both galaxy populations. Fiducially, this study ignore the bias stochasticity, shear intrinsic alignments (Hirata & Seljak 2004; Catelan, Kamionkowski & Blandford 2001), uncertainties in photo- $z$  distributions (Newman 2008; Matthews

& Newman 2010) and other shear systematics (Bernstein 2009).

The DETF figure of merit is inversely proportional to the  $(w_0, w_a)$  1- $\sigma$  contour area. Analogous Gaztañaga et al. (2012) defined an extended FoM,

$$\text{FoM}_S \equiv \frac{1}{\sqrt{\det [F_S^{-1}]}} \quad (17)$$

where  $S$  is a parameter sub-space. Parameters not in  $S$  are marginalised over. Since this concept is quite natural, other papers (e.g. Asorey et al. (2012); Kirk et al. (2013); Asorey et al. (2012)), define similar FoMs. Identical to Gaztañaga et al. (2012), we define three FoMs (in addition to DETF FoM)

- $\text{FoM}_{\text{DETF}}$ .  $S = (w_0, w_a)$ . Dark Energy Task Force (DETF) figure of merit. Inversely proportional to the error ellipse of  $(w_0, w_a)$ .
- $\text{FoM}_w$ .  $S = (w_0, w_a)$ . Equivalent to  $\text{FoM}_{\text{DETF}}$ , but instead of  $\gamma = 0.55$  from GR, the  $\gamma$  is considered a free parameter and is marginalised over.
- $\text{FoM}_\gamma$ .  $S = (\gamma)$ . Inverse error on the growth parameter  $\gamma$ , when marginalising over the other cosmological parameters and the galaxy bias. Therefore e.g.  $\text{FoM}_\gamma = 10, 100$  respectively corresponds to 10%, 1% expected error on  $\gamma$ .
- $\text{FoM}_{w\gamma}$ .  $S = (w_0, w_a, \gamma)$ . Combined figure of merit for  $w_0, w_a$  and  $\gamma$ . The 3D determinant also includes the correlation between the dark energy  $(w_0, w_a)$  and growth  $(\gamma)$  constraints.

Note that different authors introduce numerical prefactors of 1/4 (or 1/4 $\pi$ ) (Bridle & King 2007; Joachimi & Bridle 2010) in the FoM. In these papers results are often presented in  $\text{FoM}_{w\gamma}$ , while the other FoMs are used to disentangle gains in measuring expansion and growth history. One should be aware that the FoMs scale with area in the following way

$$\begin{aligned} \text{FoM}_w &\propto A \\ \text{FoM}_{\text{DETF}} &\propto A \\ \text{FoM}_\gamma &\propto A^{1/2} \\ \text{FoM}_{w\gamma} &\propto A^{3/2} \end{aligned} \quad (18)$$

when not including priors and  $A$  is the survey area. Including prior reduce the slope for small areas if the prior dominate. From numerical tests (not shown), the scaling above works well for the fiducial 14.000 sq. deg. survey.

## 2.6 Fiducial galaxy surveys

The two defined populations corresponds to a spectroscopic (Bright) and photometric (Faint) survey. Both populations are magnitude limited, although a spectroscopic survey often would select specific targets to optimise the science return. The fiducial area is 14.000 sq.deg., which is around the expected sky coverage of stage-IV surveys.

Properties of the two populations, are defined in the next two subsections, with Table 1 summarising the central values. The shape of the galaxy distributions (not density) and also galaxy bias corresponds exactly to the values in Gaztañaga et al. (2012). There the galaxy distributions was

<sup>4</sup> We use the Planck Fisher matrix file "planckfish" from <http://www.physics.ucdavis.edu/DETFast/>.

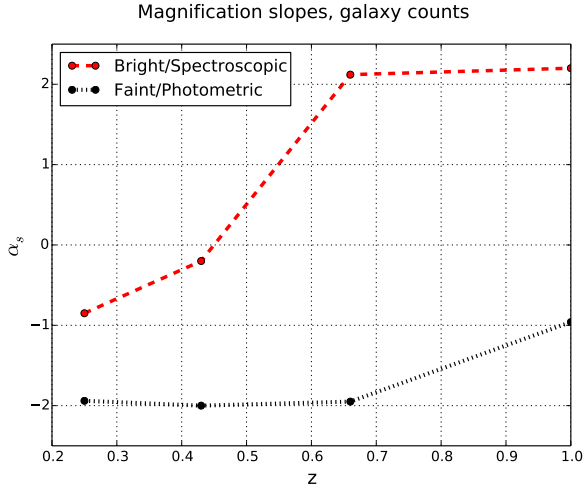


**Figure 1.** The number counts magnification slopes ( $\alpha_s$ ) for a Bright ( $18 < i_{AB} \leq 22.5$ ) and Faint ( $22.5 < i_{AB} < 24.1$ ) from the COSMOS sample. Values are extrapolated outside of this redshift range.

Parameter	Photometric (F)	Spectroscopic (B)
Area [sq.deg.]	14,000	14,000
Magnitude limit	$i_{AB} < 24.1$	$i_{AB} < 22.5$
Redshift range	$0.1 < z < 1.5$	$0.1 < z < 1.25$
Redshift uncertainty	$0.05(1+z)$	$0.001(1+z)$
z Bin width	$0.07(1+z)$	$0.01(1+z)$
Number of bins	12	71
-----		
Bias: $b(z)$	$1.2 + 0.4(z - 0.5)$	$2 + 2(z - 0.5)$
Shape noise	0.2	No shapes
-----		
density [gal/arcmin <sup>2</sup> ]	6.5	0.4
$nz - z_0$	0.702	0.467
$nz - \alpha$	1.274	1.913
$nz - \beta$	2.628	1.083

**Table 1.** Parameters describing the two surveys/populations. The first section give the area, magnitude limit, redshift range used in the forecast, redshift uncertainty modelled as a Gaussian, the redshift bin width and the resulting number of bins. In the second section is the galaxy bias ( $\delta = b\delta_m$ ) and average galaxy shape uncertainty. The third section give the galaxy density and parameters for the  $n(z)$  shape.

constructed by fitting a Smail type  $n(z)$  (Efstathiou et al. 1991)

$$\frac{dN_F}{d\Omega dz} \propto A_F \left(\frac{z}{z_0}\right)^\alpha \exp\left(-\left(\frac{z}{z_0}\right)^\beta\right) \quad (19)$$

to the public COSMOS photo- $z$  sample. In addition the magnification (see paper-I) adds the term  $\delta^{WL} = \alpha_s \delta_\kappa$ , where  $\kappa$  is the convergence, to the galaxy counts overdensities. Fig. 1 specify the fiducial magnification slopes ( $\alpha_s$ ).

### 2.6.1 Bright/Spectroscopic population

The Bright population is defined by the flux limit  $i_{AB} < 22.5$ , has a Gaussian spectroscopic redshift uncertainty of  $\sigma_{68} = 0.001(1+z)$  and the galaxy density

$$\frac{dN_B}{d\Omega dz} = A_B \left(\frac{z}{0.702}\right)^{1.083} \exp\left(-\left(\frac{z}{0.702}\right)^{2.628}\right) \quad (20)$$

over  $0.1 < z < 1.2$ . Here  $A_B$  is a normalisation amplitude and the fiducial density is  $0.4 \text{ gal/arcmin}^2$ , which is dense for a spectroscopic survey. The redshift evolution of the galaxy count bias is defined by

$$b_B(z) = 2 + 2(z - 0.5) \quad (21)$$

where  $b(0) = 1$ . To recover the radial information in the Bright/spectroscopic sample, we use  $\Delta z = 0.01(1+z)$  narrow redshift bins.

### 2.6.2 Faint/Photometric population

Weak gravitational lensing require a dense and deep sample with imaging to measure galaxy shapes. The Faint population resemble a wide field lensing survey, magnitude limited to  $i_{AB} < 24.1$  and  $\sigma_{68} = 0.05(1+z)$  Gaussian photo- $z$  accuracy. This deeper magnitude selection give the galaxy distribution:

$$\frac{dN_F}{d\Omega dz} = A_F \left(\frac{z}{0.467}\right)^{1.913} \exp\left(-\left(\frac{z}{0.467}\right)^{1.274}\right) \quad (22)$$

over  $0.1 < z < 1.4$ . The complete Faint density is  $17.5 \text{ gal/sq.arcmin}$  and in addition we only use 50% of the galaxies, which can either come from photo- $z$  quality or shear measurements cuts. Similar to the spectroscopic sample, the bias model is linear with

$$b_F(z) = 1.2 + 0.4(z - 0.5) \quad (23)$$

which also has  $b(0) = 1$ . The Faint sample use  $\Delta z = 0.07(1+z)$  thick redshift bins and contribute strongest to the WL constraints. Decreasing the bin width would not improve the radial resolution or the RSD signal, as the photo- $z$  error introduce an effective binning in redshift (Gaztañaga et al. 2012).

## 2.7 Observables

Table 2 define the notation and also give the observables included for a list of different cases. In this series of papers, a main topic is on the combined constraints from photometric (F) and spectroscopic (B) surveys, either alone (F or B) or for overlapping (FxB) or non-overlapping (F+B) areas. The "All" notation means both shear and galaxy counts, while "Counts" only includes counts. Part of the benefit of overlapping surveys come from additional cross-correlations. To quantify their impact, the second part of the table therefore present the notation for removing selected cross-correlations. Table 3 contains a list of cross-correlations which enters both directly in the text and Table 2.

Notation	Observables	Description
F:All	$\langle \delta_F \delta_F \rangle + \langle \delta_F \gamma_F \rangle + \langle \gamma_F \gamma_F \rangle$	Faint population
B:All	$\langle \delta_B \delta_B \rangle + \langle \delta_B \gamma_B \rangle + \langle \gamma_B \gamma_B \rangle$	Bright population
FxB:All	F+B:All + $\langle \delta_F \delta_B \rangle + \langle \delta_B \gamma_F \rangle$	Overlapping Faint and Bright.
F+B:All	F:All + B:All - $\langle \gamma_B \gamma_B \rangle$	Non-overlapping Faint and Bright.
FxB- $\langle \delta_B \gamma_F \rangle$ :All	F:All + B:All + $\langle \delta_B \delta_F \rangle$	FxB-All removing $\langle \delta_B \gamma_F \rangle$
FxB- $\langle \delta_F \gamma_F \rangle$ :All	B:All + $\langle \delta_F \delta_F \rangle + \langle \gamma_F \gamma_F \rangle + \langle \delta_F \delta_B \rangle + \langle \delta_B \gamma_F \rangle$	FxB-All removing $\langle \delta_F \gamma_F \rangle$
FxB- $\langle \delta \gamma \rangle$ :All	B:Counts + F:Counts + $\langle \gamma_B \gamma_B \rangle + \langle \gamma_F \gamma_F \rangle$	FxB-All. removing all cross-correlation of counts and shear.
FxB-(FB):Counts	$\langle \delta_B \delta_B \rangle + \langle \delta_F \delta_F \rangle$	FxB-Counts removing the Bright-Faint cross-correlations of counts.
FxB-(FB):All	F:All + B:All	FxB-All removing all the Bright-Faint cross-correlations, i.e. $\langle \delta_F \delta_B \rangle$ and $\langle \delta_B \gamma_F \rangle$ . Equivalent to F+B:All with covariance between F and B.

**Table 2.** Table summarizing the probe combinations and the correlations included. The first column is the notation, the second column give the correlations included and the third column is a short description. Each row correspond to a different probe combinations. The first block show standard combinations, the second block show combinations removing counts-shear correlations and the third block includes probes without cross-correlations of the two samples. Here "Counts" only include galaxy counts, while "All" also includes shear. The observables  $\langle \gamma_B \gamma_F \rangle$  and  $\langle \delta_F \gamma_B \rangle$  are also included, but not listed as their contributions are minor.

Notation	Description
$\langle \delta_F \delta_B \rangle$	Counts-Counts cross-correlations of the two galaxy populations. Important for sample variance cancellation.
$\langle \delta_B \gamma_F \rangle$	Counts-Shear cross-correlations of foreground spectroscopic galaxy counts and shear.
$\langle \gamma_B \gamma_B \rangle$	Shear-Shear for the Bright galaxies. In overlapping surveys the Bright galaxies is a subset of the photometric survey. This term is of minor importance since the Bright sample is shallower and less dense.

**Table 3.** Notation for different cross-correlations. First column give the cross-correlation and the second column is a short description.

### 3 RESULTS

In this section we investigate the combined constraint from galaxy counts and shear, treating each survey as a separate galaxy population. The first five subsections compare how different effect as RSD, BAO, lensing and intrinsic correlations contribute to the forecast. In the last subsection we present the main forecast table and discuss the relative contribution of each effect and the impact with overlapping photometric and spectroscopic surveys. Last we look at the effect of magnification. Contour plots can be found in appendix B.

#### 3.1 Auto versus cross-correlations

This subsection study how the galaxy clustering and lensing observables affects the forecast. The significant correlations for close redshift bins are the shear-shear  $\langle \gamma \gamma \rangle$  and counts-counts  $\langle \delta \delta \rangle$  correlations. Here the counts-counts correlation of the spectroscopic sample include a strong RSD signal and

intrinsic cross-correlation between nearby redshift bins. For large redshift bin separation the counts-shear  $\langle \delta \gamma \rangle$  cross-correlations are the strongest. To separate the contribution from different cross-correlations, we introduce the variable  $\Delta Z_{\text{Max}}$ . All correlations  $C_{ij}$  are required to satisfy

$$|z_j - z_i| \leq \Delta Z_{\text{Max}} \quad (24)$$

where  $z_i, z_j$  respectively are the mean of redshift bin  $i$  and  $j$ . This requirement only applies when specified for the figures. Which cross-correlations enters is discussed together with the forecast results in the next paragraphs.

The auto-correlations are always included from the  $\Delta Z_{\text{Max}}$  definition, which for probes with lensing includes the shear-shear auto-correlations. In Fig. 2 this shows at  $\Delta Z_{\text{Max}} = 0$  as a gap between lines which includes shear (All) or not (Counts). The lensing with its broad kernel can be seen to better measure dark energy (top panel, also includes  $\gamma$ ) than the growth of structure (bottom panel). Overall, galaxy shear lead to 4-5 times improvement for the combined figure of merit (FoM $_{w\gamma}$ ). In the region  $0.01 < \Delta Z_{\text{Max}} < 0.1$  the forecast also include cross-correlations between Bright/spectroscopic redshift bins, with a significant jump when including the cross-correlation with the adjacent bin. These cross-correlations contribute significantly and are studied in later subsections in the context of the Limber approximation (3.2), RSD (3.4) and BAO (3.5).

The FxB- $\langle \delta \gamma \rangle$  lines are the forecast of FxB:All without count-shear correlations. At larger  $\Delta Z_{\text{Max}}$  the counts-shear lensing becomes important, which can be seen from FxB:All and F+B:All having higher FoM $_{w\gamma}$  than FxB- $\langle \delta \gamma \rangle$ . Note that higher  $\Delta Z_{\text{Max}}$  also includes shear-shear tomography, which also enters in FxB- $\langle \delta \gamma \rangle$ . Another lensing effect is the magnification of the galaxy counts (paper-I). Intrinsic clustering dominated the counts-counts signal at low redshift separation, while magnification only becomes important at higher separations where the intrinsic correlation also van-

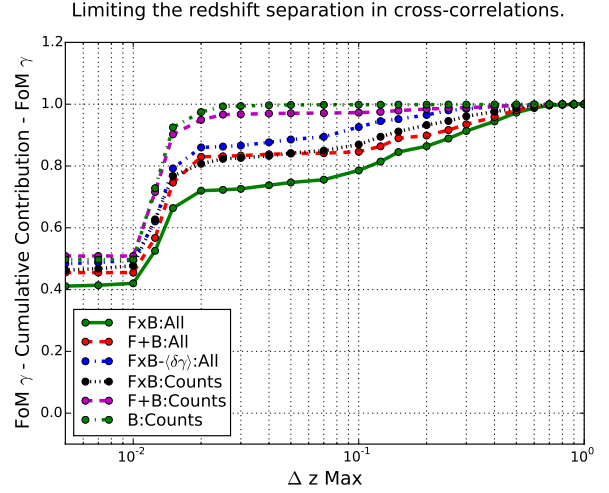
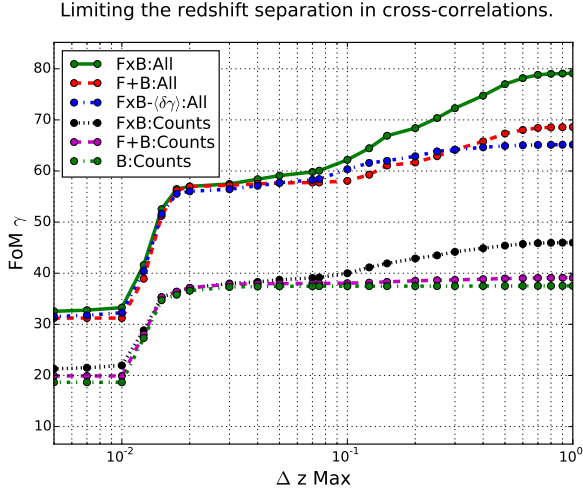
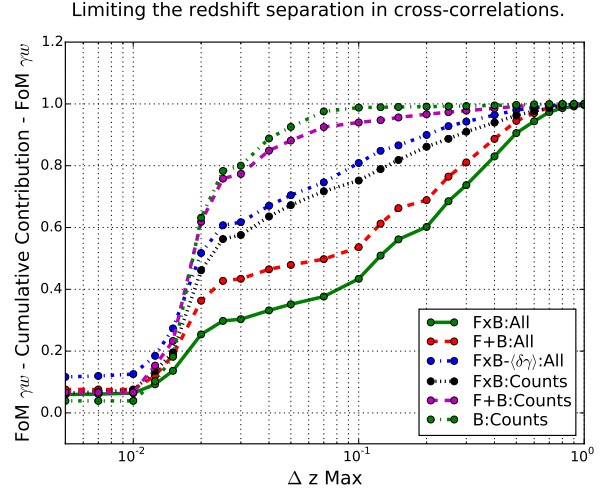
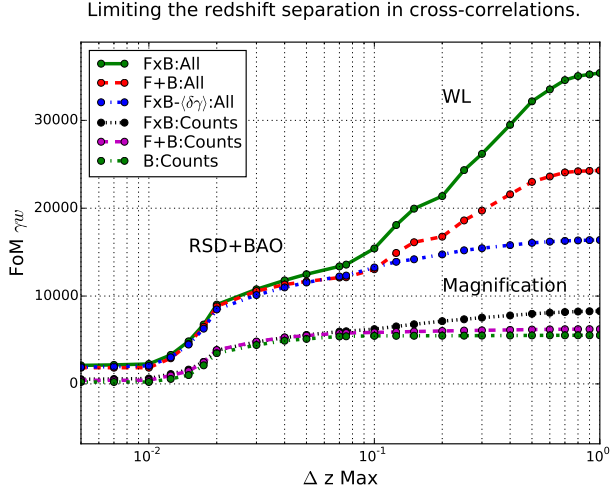


**Figure 2.** The FoM dependence on the maximum redshift separation for cross-correlations included in the forecast ( $\Delta Z_{\text{Max}}$ ). Lines corresponds to the probes FxB:All, F+B:All, FxB- $(\delta\gamma)$ :All, FxB:Counts, F+B:Counts and B:Counts. The top and bottom panel respectively corresponds to  $\text{FoM}_{w\gamma}$  and  $\text{FoM}_{\gamma}$ .

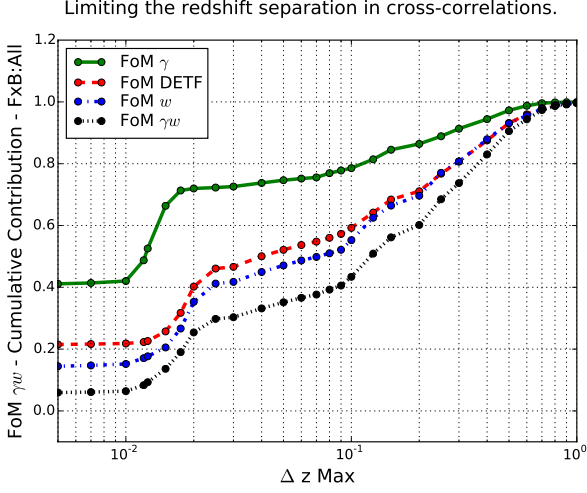
ish. The separation of FxB:Counts and F+B:Counts at high  $\Delta Z_{\text{Max}}$  is due to magnification. Magnification is also included in F and B, but the impact is strongest for the combined overlapping samples. In subsection 3.7, we study the effect of magnification when the surveys both include galaxy counts and shear.

Fig.3 shows the FoM normalized to  $\text{FoM}(\Delta Z_{\text{Max}} = 1) = 1$  where the gain has saturated. The same information is already presented (Fig. 2), but these plots are better to discuss the relative contribution of different correlations. In  $\text{FoM}_{w\gamma}$  (top panel) there is large spread between the lines. For B:Counts mostly close ( $\Delta Z_{\text{Max}} < 0.1$ ) correlations are important. When including magnification (FxB:Counts) or the shear-shear tomography (FxB- $(\delta\gamma)$ ), there is some more benefit from cross-correlations of widely separated redshift bins. The bottom lines are FxB:All and F+B:All where counts-shear contribute significantly and many different correlation types contribute to the constraints. There is much

**Figure 3.** Normalized cumulative FoM contributions for different probes. The x-axis is  $\Delta Z_{\text{Max}}$  and the FoMs are normalized by  $\text{FoM}(\Delta Z_{\text{Max}} = 1) = 1$ . Each line is a probe and the two panels show the result for different FoMs.

less difference for  $\text{FoM}_{\gamma}$  (bottom panel), where the auto-correlations account for 40-50% for all probes. For B:Counts the intrinsic counts-counts correlation between bins provide the rest, while FxB:All has a 25% contribution from counts-shear lensing.

Fig.4 is similar to Fig. 3, but compares the normalized cumulative constraints of FxB:All for the different FoMs:  $\text{FoM}_{\gamma}$ ,  $\text{FoM}_{\text{DETF}}$ ,  $\text{FoM}_w$  and  $\text{FoM}_{w\gamma}$  in the same plot. The  $\text{FoM}_{\gamma}$  line depends strongest on the auto-correlation. This is expected as the galaxy clustering (counts-counts) is important for measuring the growth. Interestingly the next two lines are  $\text{FoM}_{\text{DETF}}$  and  $\text{FoM}_w$ , while  $\text{FoM}_{w\gamma}$  which includes both dark energy and the growth ( $\gamma$ ) benefit the most from different correlations. Also, fixing the bias change which correlations that contribute (plot not shown), while keeping the FoM/line order. How marginalising over the bias change the forecast is an important part of this paper and is studied further in paper-III.



**Figure 4.** Normalized cumulative FoM contributions for different probes. The x-axis is  $\Delta Z_{\text{Max}}$  and the FoMs are normalized by  $\text{FoM}(\Delta Z_{\text{Max}} = 1) = 1$ . All results are for FxB:All and the lines corresponds to  $\text{FoM}_{\gamma}$ ,  $\text{FoM}_{\text{DETF}}$ ,  $\text{FoM}_w$  and  $\text{FoM}_{\gamma w}$ .

### 3.2 Limber approximation

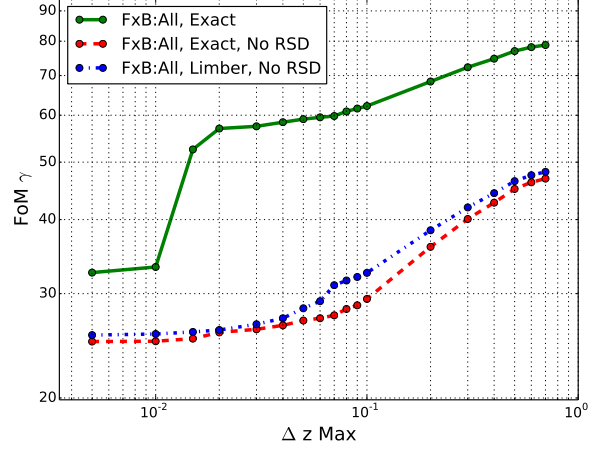
Paper-I compared the correlations estimated using the exact calculations to the correlations when using the Limber approximation. For narrow redshift bins of  $\Delta z = 0.01(1+z)$ , the Limber approximation can overestimate the galaxy counts auto-correlations by a factor of 2-3. Further, in the Limber approximation there is no counts-counts cross-correlations between non-overlapping redshift bins, which is not a good approximation for  $\Delta z = 0.01(1+z)$  wide bins in the Bright sample.

Fig.5 compare the exact calculations with the Limber approximation. Included in the panels is one line showing the exact calculations with RSD, while the other two lines are the exact calculation and Limber approximation in real space (No RSD). The redshift space distortion signal in the correlation is powerful, especially in measuring  $\gamma$ . Comparing the three lines show how cross-correlations and redshift space distortions contribute to measuring dark energy and the growth of structure. For  $\gamma$  including the cross-correlations has little effect, while the redshift space distortions improve  $\text{FoM}_{\gamma}$  for FxB:All by 70%. On the other hand, for  $\text{FoM}_{\text{DETF}}$  the cross-correlations of galaxy count in the radial direction is powerful, while the RSD signal contributes little. One can understand the main traits from the amplitudes and shapes of the correlations. The  $\gamma$  parameter changes the clustering amplitude, while dark energy parameters  $\omega$  more directly affects the shape.

For  $\text{FoM}_{\text{DETF}}$  without RSD (real space) the exact calculations and Limber approximation results cross around  $\Delta Z_{\text{Max}} = 0.015$ . The width of the spectroscopic redshift bins here is  $\Delta z = 0.01(1+z)$  and around the crossing the exact calculations begin to include correlations with nearby redshift bins. These are important for dark energy constraints (subsection 3.5). Also, similar to  $\text{FoM}_{\gamma}$ , when counts-shear becomes important at large  $\Delta Z_{\text{Max}}$ , the difference decreases because of the smaller error in Limber approximation.

The higher galaxy counts auto-correlations in the Lim-

Comparing the Exact correlations and the Limber approximation.



Comparing the Exact correlations and the Limber approximation.

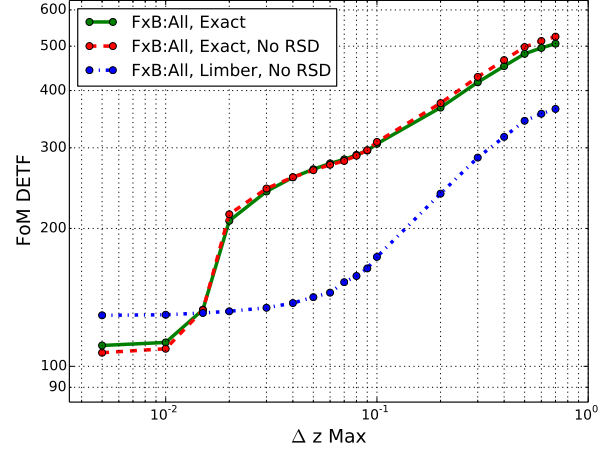


**Figure 5.** Forecast for FxB:All using the exact calculations and the Limber approximation. The first two lines respectively show the FoM in redshift and real space, while the last use the Limber approximation in real space. The top and bottom panel respectively show  $\text{FoM}_{\gamma}$  and  $\text{FoM}_{\text{DETF}}$ .

ber approximation reduce the impact of shot-noise. One can in Fig. 5 see how the  $\text{FoM}_{\gamma}$  line in top panel of Fig.5 is slightly lower for the Exact calculation than the Limber approximation. For larger  $\Delta Z_{\text{Max}}$ , the lines first diverge before converging when also including counts-shear cross-correlations (high  $\Delta Z_{\text{Max}}$ ). While the Limber approximation is accurate for the counts-shear signal, the higher galaxy counts lead to an overestimated error (see Eq. 15). As a result, the counts-shear correlations contribute less in the Limber approximation.

### 3.3 Resolution in redshift

Increasing the number of spectroscopic bins result in better constraints. The redshift bin width in a 2D forecast corresponds approximately to the maximum scale  $k_{\text{max}} = 2\pi/\lambda_{\text{min}}$ , where  $\lambda_{\text{min}}$  is the comoving width of the redshift bins (Asorey et al. 2012). The gain for small enough bins

Effect of covariance for the Bright/spectroscopic sample.

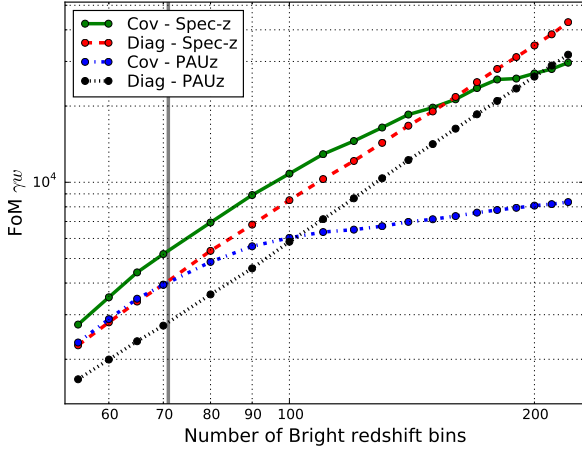


**Figure 6.** Effect of the covariance and photo-z. The lines all show  $\text{FoM}_{w\gamma}$  for galaxy counts for the spectroscopic sample, with the number of bins varying on the x-axis. Two lines (cov) include the full covariance, while the other two (only diag) only use the variance. Each of these configuration is run either using spectroscopic redshifts (spec-z) or narrow band photometry (PAUz,  $\sigma_{68}/(1+z) = 0.0035$ ). A vertical line mark the fiducial number of spectroscopic redshift bins (71).

when increasing the number of bins therefore mainly come from probing smaller scales. Note that having such a large number of bins can lead to include more nonlinear modes in the radial direction than in the angular direction. To be consistent we need to limit the number of radial bins to the corresponding  $l_{\text{max}}$  scale (see Asorey et al. (2012); Asorey, Crocce & Gaztañaga (2014)). In our case  $N_z = 70$  is the corresponding number and in this regime PAUz is quite close to Spec-z. In this section we are not comparing to a 3D forecast, but focus on the effect of the covariance between the observables.

Fig. 6 show  $\text{FoM}_{w\gamma}$  for an increasing number of bins, where the bin width  $\Delta z = w(1+z)$  is set by the number of redshift bins<sup>5</sup>. Focusing first on the result for many redshift bins, one expect the covariance to be important for increasingly thinner bins. The galaxy density per bin also decrease, but the fiducial sample is dense (0.4 gal/sq.arcmin) and the effect of shot-noise is less important (plot not shown). Assume the auto-correlations are close to equal in two bins ( $C_{AA} \approx C_{BB}$ ) and define  $\alpha \equiv C_{AB}/C_{AA}$ . The Pearson cor-

<sup>5</sup> Let  $z_i$  denote the edges between redshift bins and where  $z_0$  is the start of the redshift range. A frequently used redshift binning is  $z_n = z_{n-1} + (1 + z_{n-1}) * w$  where the constant  $w$  give the bin width. Provable by mathematical induction, then

$$z_n = (1 + z_0)(1 + w)^n - 1. \quad (25)$$

is the  $n$ th edge between the redshift bin. For a binning  $\Delta z = w(1+z)$ , then

$$w = \sqrt[N]{\frac{1 + z_{\text{Max}}}{1 + z_0}} - 1 \quad (26)$$

divide the interval  $[z_0, z_{\text{Max}}]$  in  $n$  bins into  $N$  redshift bins.

relations,  $R[A, B] = \text{Cov}(A, B) / \sqrt{\text{Var}[A] * \text{Var}[B]}$ , for the covariance matrix (Eq.15) is then

$$R[\text{Auto}(AA), \text{Auto}(BB)] \approx \alpha^2 \quad (27)$$

$$R[\text{Auto}(AA), \text{Cross}(AB)] \approx \alpha\sqrt{2}/\sqrt{1+\alpha} \quad (28)$$

when ignoring the shot-noise. From these equation, the covariance increase for thinner bins which has higher  $\alpha$  (see paper-I). The largest covariance is not between auto-correlations, but between the auto and cross-correlations. Previous studies expected the covariance to saturate the result, but could not demonstrate this due to technical difficulties with many bins<sup>6</sup> (Asorey et al. 2012; Di Dio et al. 2013). In Fig. 6 the covariance limits the results, with the lines being even flatter (and numerical unstable) when approaching 300 bins. The forecast also saturate for  $\text{FoM}_w$ ,  $\text{FoM}_\gamma$  and  $\text{FoM}_{\text{DETF}}$  (not shown). For PAUz the forecast FoMs become flat earlier (less bins), since the photo-z also correlate the fluctuations in the different redshift bins.

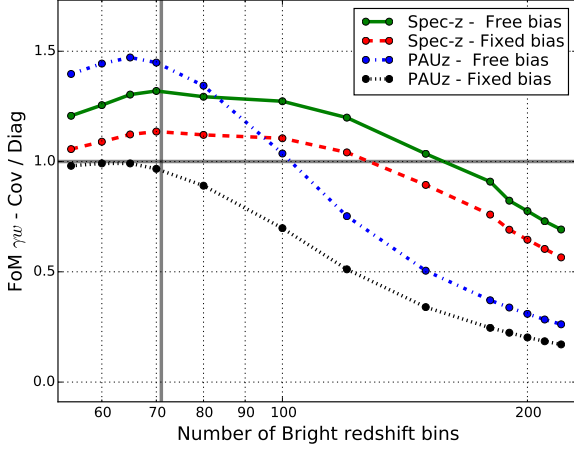
For an intermediate low number of bins (50-100), the covariance between observables increase  $\text{FoM}_{w\gamma}$ . This result is counter-intuitive, but is similar to the sample variance cancellations for multiple galaxy tracers. When two observables depend differently on nuisance parameters (e.g. bias), the covariance between the observables introduce a covariance between the nuisance parameters. The additional covariance between the bias parameters reduce their freedom, which increase cosmological constraints when marginalised over. The covariance naturally also reduce the information, since the observables are no longer independent. If the forecast improve or degrade depends on the details of these competing effects (see Eriksen & Gaztanaga (2014a)).

Fig. 7 show the  $\text{FoM}_{w\gamma}$  ratio between including the full covariance or only the diagonal entries (variance). For spectroscopic redshifts and marginalising over the bias (free bias), the covariance increase  $\text{FoM}_{w\gamma}$  until about 160 spectroscopic bins. This show that the covariance between different redshift slices increase constraints through reduced the sample variance. When fixing the bias the gain is about 3 times lower, but it is still a 10% effect. We attribute this to a changed covariance between the cosmological parameters, some of which we marginalise over. While the constraints can be higher for only the variance, the covariance should be included in parameter fits to not bias the results. With narrow band photo-z (PAUz), the effect of the covariance change. For a free bias the gain is higher, while there is no benefit when fixing the bias.

How does the same-sky (FxB/F+B) conclusions depend on the number of spectroscopic bins? Fig. 8 show the combined forecast (FxB, F+B) for the fiducial case, which use spectroscopic redshift and include the covariance. The Bright sample (Fig. 8) benefit from more redshift bins. This however also increase the number of counts-counts cross-correlations with the photometric sample and cross-correlations of spectroscopic galaxy counts with shear. For

<sup>6</sup> In this subsection the forecast exclude all counts-counts cross-correlations  $C_{ij}$  with  $0.1 < |z_j - z_i|$  for redshift bins  $i, j$ . These include little cosmological information (see magnification subsection 3.7) and removing these help to reduce the dimension of the covariance matrix.

Gain from the covariance for an increasing number of bins.



**Figure 7.** The gain from the covariance. The figure show the forecast ratio between including the full covariance or only the diagonal entries. All lines show  $\text{FoM}_{w\gamma}$  for the Bright sample using galaxy counts (B-Counts) as a function of redshift bins. Two lines use a spectroscopic sample (spec-z), while the other two use narrow-band photo-z sample (PAUz). For two lines we marginalise over the bias (free bias), while for the other two the bias is fixed (fixed bias). A vertical line mark the fiducial number of spectroscopic redshift bins (71).

Effect of covariance for different probes.

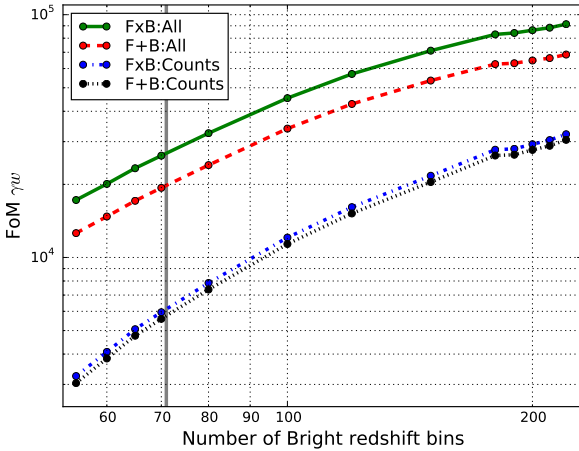


**Figure 8.** The forecast for different probes and increasing number of bins. On the x-axis is the number of spectroscopic redshift bins, while the lines show  $\text{FoM}_{w\gamma}$  for the probe combinations FxB:All, F+B:All, FxB:Counts and F+B:Counts. A vertical line mark the fiducial number of spectroscopic redshift bins (71).

both "All" and "Counts" the FxB/F+B ratio is nearly constant over a wide number of spectroscopic redshift bins. This shows our conclusions on the same-sky issue is quite robust with respect to the number of redshift bins.

The RSD/no-RSD forecast ratio, increasing number of bins.

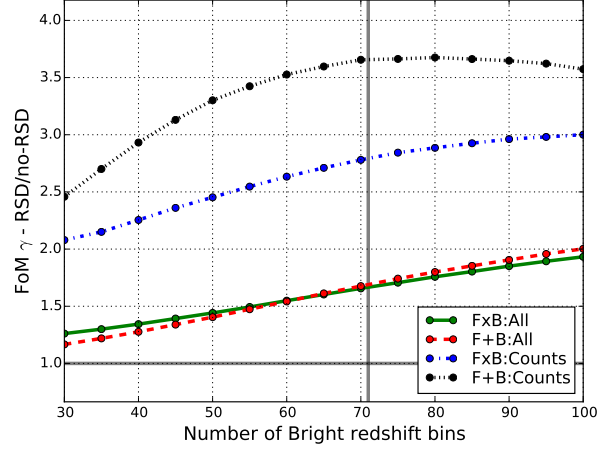


**Figure 9.** The  $\text{FoM}_{\gamma}$  ratio between a redshift and real space forecast when varying the number of spectroscopic redshift bins. A vertical line mark the fiducial number of spectroscopic redshift bins (71). The four lines corresponds to FxB:All, F+B:All, FxB:Counts and F+B:Counts.

### 3.4 Redshift space distortions (RSD)

Redshift space distortions affects the overdensities of galaxies. A matter overdensity attract galaxies, which change their velocities and introduce a change in redshift. At linear level, the change in galaxy count overdensities is the Kaiser effect. The redshift space galaxy spectrum  $\tilde{P}_{\text{Gal}}(k)$  is then

$$\tilde{P}_{\text{Gal}}(k, \mu) = (b + \mu^2 f)^2 P(k) \quad (29)$$

where  $P(k)$  is the real space matter power spectrum,  $b$  is the galaxy bias,  $\mu$  is the cosine of line of sight angle and  $f \equiv \Omega_m(z)^\gamma$ . In the forecast, the RSD effect enters in the 2D correlations. Overdense regions attract nearby galaxies, which can move galaxies between redshift bins. This effect often increase the amplitude of the 2D-correlations (see paper-I).

The redshift space distortions is a powerful effect for measuring  $\gamma$ . Fig. 9 show how including RSD in the correlations improves  $\text{FoM}_{\gamma}$  by a factor between 1.5 and a few. For the other  $\text{FoM}$ s (not shown) RSD decrease the result with 0-5%. Now we first focus on the results for counts. Observing galaxy counts over separate skies (F+B:Counts) is the combination which benefits most from RSD. For only B:Counts (not shown), the RSD improves for the fiducial binning the constraints with a factor of 3.9. The added RSD component is independent of bias, and therefore reduce the degeneracies between  $\gamma$  and the bias. In FxB:Counts, the surveys are overlapping and the samples (F and B) can be cross-correlated. The cross-correlations and also sample variance cancellation directly from overlapping volumes (subsection 3.6) improve bias constraints and RSD is therefore less important for FxB:Counts.

One should note, comparing models with and without RSD in the angular correlations is slightly misleading. The forecast in redshift space or real space includes the same correlations and only differ by including the RSD component in

the correlations. One can therefore not assume RSD always improves the parameter constraint, but the benefit depends largely on the resulting correlations between the parameters. As seen in last paragraph, the measurement of  $\gamma$  improves greatly from RSD. On the other hand, in the theoretical real space angular correlations, there is radial information in the cross-correlations between redshift bins. Including RSD will, as we will see, reduce the dark energy constraints from intrinsic galaxy counts cross-correlations with nearby redshift bins.

When including shear the importance of RSD naturally decrease (Fig.9, FxB:All and F+B:All). These probes also include the shear-shear signal, which is unaffected by the RSD. Even if the ratios are lower, the factor of 2 is still a good improvement. Since F+B:Counts benefit more than FxB:Counts from RSD, the separation between F+B:All and FxB:All is smaller than expected. One can understand this from looking at the counts-shear variance. The variance for the cross-correlation of a foreground galaxy counts ( $\delta_i$ ) density with background shear ( $\gamma$ ) is (see Eq. 15)

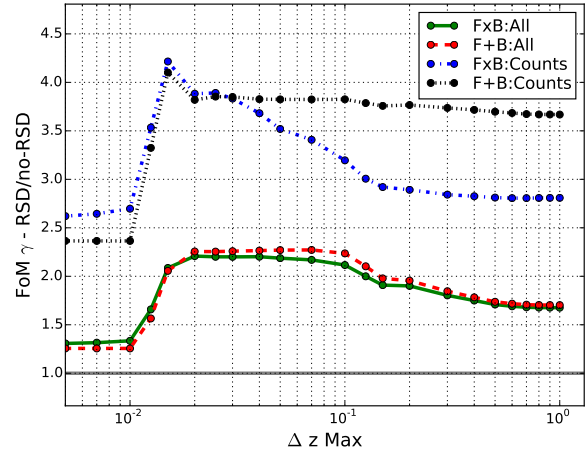
$$\text{Var}(\langle \delta_i \gamma \rangle) = N^{-1}(l)[\langle \delta_i \delta_i \rangle \langle \gamma \gamma \rangle + \langle \delta_i \gamma \rangle^2] \quad (30)$$

where  $N(l)$  is the number of modes. The  $\langle \delta_i \gamma \rangle$  signal and the second term in the variance is approximately independent of redshift space distortions. On the other hand, the  $\langle \delta_i \delta_i \rangle$  auto-correlations increase strongly from RSD. Since the error increases, including RSD in the forecast reduce the importance of counts-shear.

Top panel of Fig.10 shows how including RSD affects the forecasts. Instead of studying the FoMs as a function of number of redshift bins, this figure use the fiducial binning and vary  $\Delta Z_{\text{Max}}$ . Subsection 3.1 explained how  $\Delta Z_{\text{Max}}$  can be used to distinguish between contributions from auto-correlations, cross-correlation with nearby redshift and counts-shear weak lensing. The largest RSD effect is for  $\text{FoM}_\gamma$  and F+B:Counts increase by a factor of 3.6 with respect to the real space forecast. When including cross-correlations between nearby bins, the importance of RSD increase for all probe combinations. In paper-I we showed how RSD affect the auto and cross-correlations differently, which here improve the growth constraints. For FxB:Counts, higher  $\Delta Z_{\text{Max}}$  also include weak lensing magnification. Magnification adds an additional bias measurement, therefore decreasing the impact of redshift space distortions.

Last, the  $\text{FoM}_{\text{DETF}}$  (Fig.10, bottom panel) include some interesting trends. For the auto-correlation the RSD improve the dark energy constraints. Around  $0.01 < \Delta Z_{\text{Max}} < 0.02$  the forecast also include galaxy counts cross-correlations between spectroscopic redshift bins. Then the  $\text{FoM}_{\text{DETF}}$  ratio suddenly drops because the RSD suppress the cross-correlation with nearby redshift bins, which are important for dark energy constraints. Since FxB:Counts depend stronger than F+B:Counts on magnification, the lines separate at high  $\Delta Z_{\text{Max}}$ . The magnification signal, which has similar covariance to counts-shear and benefit from RSD reducing amplitude of the auto-correlations. Since FxB:Counts depends stronger on magnification than F+B:Counts, the lines separate at high  $\Delta Z_{\text{Max}}$ .

The RSD/no-RSD forecast ratio, including more cross-correlations.



The RSD/no-RSD forecast ratio, including more cross-correlations.

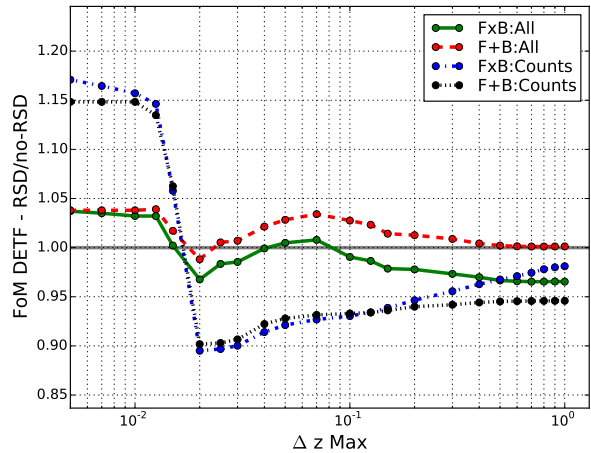


**Figure 10.** FoM ratio between redshift and real space when varying the largest redshift separations in the cross-correlations ( $\Delta Z_{\text{Max}}$ ). In the two plots corresponding to  $\text{FoM}_\gamma$  and  $\text{FoM}_{\text{DETF}}$  the four lines are the probes FxB:All, F+B:All, FxB:Counts and F+B:Counts.

### 3.5 Baryon Acoustic Oscillation (BAO)

In the observed galaxy distribution BAO is a characteristic scale ( $\sim 150$  Mpc today), which is measurable both in the transverse/angular and radial/redshift direction (Gaztañaga, Cabré & Hui 2009; Reid et al. 2012). Observing the BAO can therefore probe cosmology by measuring the comoving and angular diameter distance. Accurately predicting the power spectrum is done by solving the Boltzmann equation. The Eisenstein-Hu analytical power spectrum formula we use here is less accurate, but can be estimated the power spectrum both only with the continuum and including the BAO wiggles. In this subsection we compare the forecasts with and without the BAO feature.

Fig. 11 show in the top panel the ratio between including or not the BAO (BAO/no-BAO) for different number of spectroscopic redshift bins. For the fiducial binning (71 bins), the  $\text{FoM}_{\text{DETF}}$  improve with 20-30%, while  $\text{FoM}_\gamma$  only change with  $\pm 2\%$  (not shown). This trend is oppo-

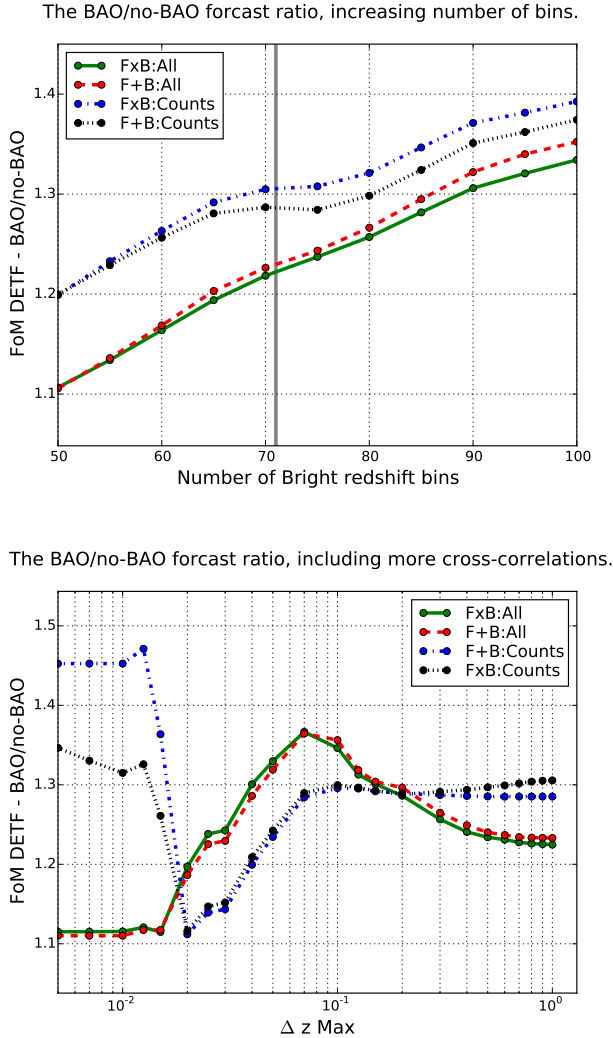


**Figure 11.** Effect of including BAO wiggles. The ratio divides the fiducial forecast on one removing the BAO wiggles in the Eisenstein-Hu power spectrum. In the top and bottom panel, the  $\text{FoM}_{\text{DETf}}$  is respectively shown when varying the number of spectroscopic redshift bins and  $\Delta Z_{\text{Max}}$ . The four lines are for the probes FxB:All, F+B:All, FxB:Counts and F+B:Counts. A vertical line in the upper panel corresponds to the fiducial number of spectroscopic redshift bins (71).

site to RSD, discussed in subsection 3.4, where RSD contributed strongly to  $\gamma$  constraints ( $\text{FoM}_{\gamma}$ ), but only gave minor changes to the dark energy constraints ( $\text{FoM}_{\text{DETf}}$ ). Measuring  $\gamma$  depends on measuring the amplitude, while the dark energy constraints come more from the power spectrum shape measurements (BAO position as opposed to amplitude). The RSD breaks the degeneracy between the galaxy bias and the growth parameter ( $\gamma$ ). On the other hand, the BAO introduce a known distance scale, which is more suited to measure the shape and expansion history.

The BAO peak can in configuration space be modelled by a 30 Mpc/h wide Gaussian. For the fiducial binning (71 bins), the bin width at  $z = 0.5$  is 35 Mpc/h. When increasing the number of bins, one decrease the redshift bin width, which leads to a more precise location of the BAO

peak. Thinner bins can also, as we will discuss, better measure the radial BAO in the cross-correlations between nearby bins. As a result, we find the  $\text{FoM}_{\text{DETf}}$  BAO/no-BAO ratio to around double when using 100 instead of 71 bins in the spectroscopic sample.

Fig. 11, bottom panel, show the BAO/no-BAO ratio when increasing  $\Delta Z_{\text{Max}}$ . The forecast only include auto-correlations when  $\Delta Z_{\text{Max}} = 0$ , while  $0.01 \leq \Delta Z_{\text{Max}}$  also has the cross-correlations between redshift bins. For only auto-correlations of galaxy counts, the ratio is artificially high since the forecast use one bias parameter per redshift bins and population. The "Counts" ratios therefore drops when including the cross-correlations between close redshift bins. Previously paper-I found a stronger BAO signal in the cross-correlation between nearby bins than in the auto-correlation. This was caused by the cross-correlation selecting galaxy pairs with a given radial distance, therefore suppressing the small-scale information. For both "All" and "Counts" the BAO/no-BAO ratio grows from 1.1 to 1.3-1.35, showing that radial BAO is an important contribution.

The shear-shear auto-correlations are in "All" included for all  $\Delta Z_{\text{Max}}$  values. When including lensing the BAO/no-BAO ratio increase is higher with  $\Delta Z_{\text{Max}}$ , since the BAO help to break degeneracies. For higher  $0.1 < \Delta Z_{\text{Max}}$  counts-shear becomes important and the ratio again decrease. Since the ratio also decrease for a fixed bias (not shown), the decrease does not result from count-shear providing an additional bias measurement, but from the counts-shear signal depending more weakly on BAO. Because the galaxy counts magnification is a weak effect (see subsection 3.7), the lines for only counts remains quite flat for  $\Delta Z_{\text{Max}} > 0.1$ .

### 3.6 Combining WL, RSD and BAO

Previous subsections studied in detail the separate benefits of the covariance, RSD, WL and BAO. This subsection build on those and compares the relative impact of each physical effect, including knowledge of galaxy bias and sample variance cancellations. The main results are presented in four tabulars, corresponding to  $\text{FoM}_{w\gamma}$ ,  $\text{FoM}_{\gamma}$ ,  $\text{FoM}_{\text{DETf}}$  and  $\text{FoM}_w$ . For layout reasons,  $\text{FoM}_{w\gamma}$  and  $\text{FoM}_{\gamma}$  are shown in Table 4, while  $\text{FoM}_{\text{DETf}}$  and  $\text{FoM}_w$  are included in Table 5. Each row corresponds to a different probe and dashed lines divide the rows into five sections. The first two sections quantify the benefit of overlapping photometric and spectroscopic galaxy surveys. In the third section we study the single population, while the fourth and fifth section present special cases (see Table 2). On the columns are the forecast for a free/fixed galaxy bias and when removing different effects.

The first three rows of Table 4 show the forecast for FxB:All, F+B:All and the same-sky benefit: FxB/F+B. For  $\text{FoM}_{w\gamma}$  we find a 50% same-sky gain, which corresponds to 30% increase in area (Eq. 18). The origin of this benefit in  $\text{FoM}_{w\gamma}$  is explained in a companion paper (Eriksen & Gaztanaga 2014a). Here we focus on describing the different results in detail. In the dark energy FoMs ( $\text{FoM}_w$  and  $\text{FoM}_{\text{DETf}}$ ) the benefit is similar, while the  $\text{FoM}_{\gamma}$  ratio is 1.1, which corresponds to a 20% larger area. While the details differ, for galaxy counts and shear we find similar benefits from overlapping photometric and spectroscopic surveys. In general, the absolute numbers in the forecast

$10^{-3}$ FoM $\gamma_w$	Fiducial	xBias	No Magn	No WL	No RSD	No BAO	No WL-xBias	No RSD-xBias	No BAO-xBias
FxB:All	35.5	213	35.1	7.32	17.1	27.8	59.1	163	206
F+B:All	24.3	193	24.2	6.13	11.0	18.0	61.5	155	183
Improvement	1.5	1.1	1.4	1.2	1.6	1.6	0.96	1.1	1.1
FxB:Counts	8.29	61.9	7.32	7.32	3.31	6.00	59.1	50.2	48.0
F+B:Counts	6.24	62.0	6.13	6.13	1.72	4.41	61.5	53.2	44.6
Improvement	1.3	1.00	1.2	1.2	1.9	1.4	0.96	0.94	1.1
F:All	3.10	51.2	3.07	0.064	2.61	2.77	2.68	52.0	53.2
B:All	7.91	52.6	7.91	5530	2.76	5.42	45.4	42.6	43.1
F:Counts	0.077	2.85	0.064	0.064	0.036	0.050	2.68	2.93	2.34
B:Counts	5.53	45.4	5530	5.53	1.45	3.78	45.4	37.9	31.6
FxB- $\langle\delta_F\gamma_F\rangle$ :All	32.4	201	32.3	7.32	15.4	25.3	59.1	152	194
FxB- $\langle\delta_B\gamma_F\rangle$ :All	33.8	208	33.4	7.32	16.2	26.3	59.1	160	201
FxB- $\langle\delta\gamma\rangle$ :All	16.4	100	16.1	7.32	7.46	12.0	59.1	79.2	89.6
FxB- $\langle$ FB $\rangle$ :All	30.7	199	30.4	6.05	14.1	23.3	55.4	154	191
FxB- $\langle$ FB $\rangle$ :Counts	6.58	57.1	6.05	6.05	2.02	4.67	55.4	47.3	43.1
(FxB- $\langle$ FB $\rangle$ )/F+B):All	1.3	1.0	1.3	0.99	1.3	1.3	0.90	0.99	1.1
(FxB- $\langle$ FB $\rangle$ )/F+B):Counts	1.1	0.92	0.99	0.99	1.2	1.1	0.90	0.89	0.96
FoM $\gamma$	Fiducial	xBias	No Magn	No WL	No RSD	No BAO	No WL-xBias	No RSD-xBias	No BAO-xBias
FxB:All	79	159	79	42	47	80	156	115	161
F+B:All	69	162	69	39	40	67	158	119	163
Improvement	1.1	0.99	1.1	1.1	1.2	1.2	0.98	0.97	0.99
FxB:Counts	46	156	42	42	16	47	156	109	150
F+B:Counts	39	158	39	39	11	39	158	112	149
Improvement	1.2	0.98	1.1	1.1	1.5	1.2	0.98	0.97	1.0
F:All	40	68	40	7.4	39	41	56	65	69
B:All	45	147	45	38	15	45	147	102	145
F:Counts	8.1	56	7.4	7.4	5.3	7.8	56	53	57
B:Counts	38	147	38	38	9.6	38	147	102	133
FxB- $\langle\delta_F\gamma_F\rangle$ :All	78	158	78	42	45	79	156	114	160
FxB- $\langle\delta_B\gamma_F\rangle$ :All	79	159	78	42	47	80	156	115	160
FxB- $\langle\delta\gamma\rangle$ :All	65	158	65	42	31	64	156	112	159
FxB- $\langle$ FB $\rangle$ :All	76	157	76	39	46	77	153	113	158
FxB- $\langle$ FB $\rangle$ :Counts	41	153	39	39	12	42	153	107	146
(FxB- $\langle$ FB $\rangle$ )/F+B):All	1.1	0.97	1.1	1.0	1.1	1.1	0.97	0.95	0.97
(FxB- $\langle$ FB $\rangle$ )/F+B):Counts	1.1	0.97	1.0	1.0	1.1	1.1	0.97	0.95	0.98

**Table 4.** Table to compare different combinations of observables and effects. The two tabular corresponds to FoM $_{w\gamma}$  and FoM $_{\gamma}$  indicated in the upper left corner. The label column indicates the populations in the rows (B:Bright/Spectroscopic, F:Faint/Photometric) and using overlapping (x) or separate (-) skies. Counts include only overdensities of number counts, while All also include galaxy shear. The rows are divided through dashed lines in five sections. First two sections study overlapping versus non-overlapping surveys, where the last line is the fraction gained using overlapping surveys. Third row section present the single populations cases (F or B). The fourth section looks at special cases, defined in subsection 2.7, designed to understand which correlations contribute most. Fifth section is the forecast for overlapping surveys without any cross-correlations and the ratio to non-overlapping surveys. The column "Fiducial" is the fiducial forecast, while "xBias" fixes the galaxy bias. In the next columns are forecasts corresponding to removing Magnification (No Magn), Weak Lensing (No WL), Redshift Space Distortions (No RSD) and Baryonic Acoustic Oscillations (No BAO). The last three columns include fixed bias cases.

presented depends strongly on the parameterization of the galaxy bias. For example, exact knowledge of bias would increase FxB:All and F+B:All with 6.0x and 7.9x respectively. Details on the galaxy bias is studied in paper-III.

For the four defined FoMs, the survey overlap is more important when marginalising over the bias. One example is the fiducial column, where the FxB:All/F+B:All ratio for

FoM $_{w\gamma}$  decrease from 1.5 to 1.1 when fixing the galaxy bias. Also, we see a lower gain from overlapping surveys when including RSD or BAO. Those effects break degeneracies between the galaxy bias and cosmology, which increase the single population cases and therefore reduce the importance of overlapping surveys. Without lensing and for a fixed bias, we find overlapping surveys contribute negatively. This is be-

FoM $w$	Fiducial	xBias	No Magn	No WL	No RSD	No BAO	No WL-xBias	No RSD-xBias	No BAO-xBias
FxB:All	449	1340	445	172	363	347	379	1410	1290
F+B:All	355	1190	352	159	272	267	388	1310	1120
Improvement	1.3	1.1	1.3	1.1	1.3	1.3	0.98	1.1	1.1
FxB:Counts	180	397	172	172	202	129	379	462	320
F+B:Counts	159	391	159	159	161	112	388	473	300
Improvement	1.1	1.0	1.1	1.1	1.3	1.1	0.98	0.97	1.1
F:All	77	759	77	8.7	67	67	48	804	773
B:All	174	359	174	147	179	122	310	418	297
F:Counts	9.5	51	8.7	8.7	6.8	6.4	48	55	41
B:Counts	147	310	147	147	152	100	310	373	238
FxB- $\langle\delta_F\gamma_F\rangle$ :All	417	1270	416	172	343	320	379	1340	1220
FxB- $\langle\delta_B\gamma_F\rangle$ :All	429	1310	425	172	347	330	379	1390	1260
FxB- $\langle\delta\gamma\rangle$ :All	252	635	248	172	240	186	379	705	564
FxB- $\langle$ FB $\rangle$ :All	404	1270	400	156	309	302	361	1360	1210
FxB- $\langle$ FB $\rangle$ :Counts	160	372	156	156	168	112	361	443	296
(FxB- $\langle$ FB $\rangle$ )/F+B):All	1.1	1.1	1.1	0.98	1.1	1.1	0.93	1.0	1.1
(FxB- $\langle$ FB $\rangle$ )/F+B):Counts	1.0	0.95	0.98	0.98	1.1	1.0	0.93	0.94	0.99

FoM DETF	Fiducial	xBias	No Magn	No WL	No RSD	No BAO	No WL-xBias	No RSD-xBias	No BAO-xBias
FxB:All	517	1750	512	210	535	422	981	1780	1670
F+B:All	399	1640	397	196	399	324	1050	1710	1540
Improvement	1.3	1.1	1.3	1.1	1.3	1.3	0.94	1.0	1.1
FxB:Counts	219	996	210	210	223	168	981	991	883
F+B:Counts	197	1050	196	196	208	153	1050	1050	922
Improvement	1.1	0.95	1.1	1.1	1.1	1.1	0.94	0.94	0.96
F:All	205	853	204	11	207	202	261	899	863
B:All	206	842	206	180	209	148	801	844	748
F:Counts	12	263	11	11	11	8.2	261	268	261
B:Counts	180	801	180	180	196	137	801	797	696
FxB- $\langle\delta_F\gamma_F\rangle$ :All	480	1700	480	210	499	389	981	1730	1620
FxB- $\langle\delta_B\gamma_F\rangle$ :All	495	1720	491	210	515	402	981	1750	1640
FxB- $\langle\delta\gamma\rangle$ :All	311	1140	309	210	313	236	981	1150	1030
FxB- $\langle$ FB $\rangle$ :All	474	1670	471	191	497	382	949	1710	1580
FxB- $\langle$ FB $\rangle$ :Counts	196	959	191	191	207	149	949	959	842
(FxB- $\langle$ FB $\rangle$ )/F+B):All	1.2	1.0	1.2	0.97	1.2	1.2	0.91	1.0	1.0
(FxB- $\langle$ FB $\rangle$ )/F+B):Counts	1.00	0.91	0.97	0.97	0.99	0.97	0.91	0.91	0.91

**Table 5.** Same as Table 4 for FoM $_w$  and FoM $_{DETF}$ 

cause there are no additional counts-shear cross-correlations and the reduced sampling variance only works with a free bias (Eriksen & Gaztanaga 2014a).

If we focus on the FxB:All case, we see that the galaxy bias is the effect causing larger impact in the FoMs: fixing bias increases FoM $_{w\gamma}$  by a factor x6.0. For free bias, the most important probe is WL (x4.8), then RSD (x2.1) and finally BAO (x1.3). If we look at FoM $_{\gamma}$  the order is preserved WL (x1.9) and RSD (x1.7), while BAO has no impact on FoM $_{\gamma}$ . For FoM $_w$  or FoM $_{DETF}$  we see that WL is still the most important effect, but here BAO is more relevant than RSD, which makes sense as the former measures distances, while the later measures growth, which is more relevant for FoM $_{\gamma}$ . When bias is known (xBias) the FoM $_{w\gamma}$  in overlapping surveys (FxB) the relative impact of other effects is

smaller, but we have similar hierarchy of tendencies: WL (x3.6), RSD (x1.3) and BAO (x1.04). For non-overlapping surveys (F+B) and free bias the gain is smaller and both RSD (x2.2) and BAO (x1.4) become more important relative to WL (x4.0).

Second section of rows is the forecast and overlapping skies ratio only using galaxy counts. The constraints without galaxy shear is lower, with FxB-All/F+B-All being 1.4, 1.2, 1.2 and 1.2 for FoM $_{w\gamma}$ , FoM $_{\gamma}$ , FoM $_w$  and FoM $_{DETF}$ . Fixing the bias of the fiducial case (xBias), the table shows how the Improvement ratio becomes close or slightly below unity, meaning all the benefit of cross-correlating the galaxy counts comes from measuring the galaxy bias. This is different from "All" where FoM $_{w\gamma}$  and FoM $_w$ , which depends both on the DE parameters and  $\gamma$ , improve also for a fixed

bias. With shear the overlapping surveys include an additional counts-shear signal, while for counts the only benefit comes from better bias measurements. Not including RSD degrade the galaxy bias and growth determination, which is compensated when overlapping surveys which include additional cross-correlations and sample variance cancellations to better measure the galaxy bias.

The third section shows the single population constraints, with F:All and B:All respectively being the optimal (both counts and shear) constraints for the Faint and Bright population. Below are the cases F:Counts and B:Counts, which only include galaxy counts. Weak lensing is the main contribution to the Faint sample, while the Bright sample constraints are driven by galaxy clustering and RSD. This can be seen by comparing "All" and "Counts". The ratios F:(All/Counts) and B:(All/Counts) are respectively 38 and 1.4 for  $\text{FoM}_{w\gamma}$ . In our forecast the photometric sample use photo-z redshifts, which drastically reduce the contribution from RSD and intrinsic galaxy counts cross-correlations between redshift bins. The low F:Counts constraints can suggest using less the current 12 Faint bias parameters (71 for the Bright), but the constraints would still be relatively low. Also a spectroscopic survey can not measure shear (in B:All), but the Bright includes shear when being a subset of an overlapping photometric survey.

The fourth section show the forecast for FxB:All when not including various counts-shear cross-correlations (see notation Table 2). The counts-shear signal is important for the combined constraints. Comparing FxB:All to FxB- $\langle\delta\gamma\rangle$ :All, we see how  $\text{FoM}_{w\gamma}$  almost double (2.2x free bias) when including the counts-shear correlations, while the  $\text{FoM}_w$  and  $\text{FoM}_{\text{DETF}}$  greatly improve (86% and 69%, free bias). For  $\text{FoM}_\gamma$  the change is smaller and the increase is respectively 22% and 1% for a free and fixed bias. Including only either counts-shear cross-correlations of spectroscopic (FxB- $\langle\delta_F\gamma_F\rangle$ :All) or photometric (FxB- $\langle\delta_B\gamma_F\rangle$ :All) galaxy counts give comparable constraints. Removing the counts-shear cross-correlations altogether (FxB- $\langle\delta\gamma\rangle$ :All) leads to a drastic drop. We therefore conclude the counts-shear cross-correlations are important, but multiple populations include redundant information.

Last row section study the direct same-sky improvement from overlapping volumes. In addition to the extra-correlation, the overlapping volumes increase the covariance between different galaxy samples probing the same dark matter fluctuations. The additional covariance result in a larger covariance between the bias parameters. When marginalising over the bias, this can improve the constraints (Eriksen & Gaztanaga (2014a)). The volume effect is quite small for only galaxy counts, since the constraints are mainly from the Bright/spectroscopic sample. When lensing is included the overlapping volumes measure the Faint bias and therefore improve constraints through the counts-shear cross-correlations.

### 3.7 Magnification

In Table 4 and 5, the "No Magn" column remove the effect of magnification. Weak gravitational lensing increase galaxy fluxes, altering the galaxies entering into a magnitude limited sample. Foreground matter also magnify the area, which change the observed galaxy densities. These two

effects together is the weak lensing magnification with number counts. Removing magnification is done by setting the magnification slope to zero (see Fig. 1). For FxB:All the  $\text{FoM}_{w\gamma}$ ,  $\text{FoM}_w$ ,  $\text{FoM}_{\text{DETF}}$  improve 1% from magnification, while the  $\text{FoM}_\gamma$  is close to zero ( $< 0.1\%$ ). The improvement is significant when only including galaxy counts. For FxB:Counts the magnification contributes to  $\text{FoM}_{w\gamma}$ ,  $\text{FoM}_\gamma$ ,  $\text{FoM}_w$  and  $\text{FoM}_{\text{DETF}}$  with respectively 13,10,5 and 4%.

In the previous paper Gaztañaga et al. (2012), we studied the impact of magnification and recently Duncan et al. (2014) confirmed those findings. One source of confusion was the notation "MAGN", which denoted magnification combined with galaxy clustering. While stating the galaxy clustering was the main source for the constraints, the misleading labels and partly unclear text lead some readers to believe magnification had a more central role. In this paper the forecasts of galaxy counts is simply labeled "Counts" and includes galaxy clustering, RSD and magnification. Unlike the previous article, this paper also discuss the effect of magnification also when including shear. We note that magnification is potentially more effective if marginalising of additional systematics (like photo-z outliers). A detailed study of constraining lensing systematics when combining with magnification is left for future work.

## 4 CONCLUSION

The effects of galaxy clustering, redshift space distortions (RSD), weak lensing (WL) and BAO are presented for 2D angular cross-correlations of galaxy counts and shear. Building on paper-I, which presented the modelling, this paper use the Fisher matrix formalism to estimate dark energy and growth rate ( $\gamma$ ) constraints for photometric and spectroscopic surveys. The forecast use two galaxy populations, one photometric (F) and one spectroscopic (B), and analyze the spectroscopic survey in 72 narrow redshift bins to capture the radial information. All possible cross-correlations between galaxy counts and shear are included. In this paper we focus on the relative benefit of different correlations and effects as non-linear contributions, the Limber approximation, the covariance, RSD, BAO and magnification. Details on the forecast assumptions and nomenclature can be found in section 2.

To prevent entering into the strong non-linear regime, subsection 2.2 defined a criteria for which correlations to include. In appendix A we study the non-linear effect, finding our  $k_{max}$  cut to be reasonable. The next subsection(3.1) we compare the benefit of different correlations. The effect of galaxy clustering, RSD and WL all enters in the 2D correlations. To investigate their relative impact we introduce the variable  $\Delta Z_{\text{Max}}$ , which limits the maximum distance between the mean of the two redshift bins in a correlation. For  $\Delta Z_{\text{Max}} = 0$  only the auto-correlations are included, then  $\Delta Z_{\text{Max}} \approx 0.02$  also include cross-correlations between nearby bins in the spectroscopic sampling, while counts-shear and magnification only enters for higher  $\Delta Z_{\text{Max}}$ . From plotting the figures of merit (FoM) as a function of  $\Delta Z_{\text{Max}}$ , we show how the different correlations contribute. This includes the cross-correlations between nearby bins in the spectroscopic sample.

The Limber approximation is widely used to simplify

the calculation of the galaxy clustering in 2D correlation. As shown in paper-I, the Limber approximation only works in thick redshift bins. For narrow bins, which we need for the spectroscopic sample, the Limber approximation breaks down and incorrectly estimate zero cross-correlation for close redshift bins. Subsection 3.2 show the effect on the forecast. The Limber approximation overestimate the amplitude, therefore reducing the impact of shot-noise. The exact calculations give larger errors in  $\gamma$  than the Limber approximation. More importantly, the cross-correlations of galaxy counts in nearby bins are effective in constraining dark energy. Since these are zero for the Limber approximation, it leads to the exact calculation giving stronger dark energy constraints.

The subsection 3.3 study the effect of including more bins in the spectroscopic sample. For as increasing number of bins, we find the forecast is saturating from a higher covariance. This result has previously been expected, but not shown due to technical issues with a large number of bins (Asorey et al. 2012; Di Dio et al. 2013). In the spectroscopic sample, for most bin configurations (less than 160 bins) the covariance improve the forecast. This effect come from the covariance between redshift slices, which reduce the sample variance similar to a multi-tracer analysis (see Eriksen & Gaztanaga (2014a)). Lastly, we find our same-sky result to be stable over a larger number of spectroscopic bins.

In subsection 3.4 we show how RSD break the degeneracy between the galaxy bias and  $f$ , which result in better  $\gamma$  constraints. Similar to the Limber subsection, the RSD/no-RSD ratio is shown as a function of  $\Delta Z_{\text{Max}}$ . The RSD effect suppress the galaxy counts cross-correlations of close redshift bins, which reduce their constraint. For more spectroscopic redshift bins (100 instead of 72), the RSD impact increase for the combined photometric and spectroscopic surveys. This subsection also discuss how RSD minimally impacts the signal, but decrease the counts-shear constraints through increasing galaxy counts auto-correlation which enters in the error estimate.

Opposite to RSD, the BAO contribute significantly to dark energy constrains, but only has a minor impact on  $\gamma$  constraints. Subsection 3.5 show, similar to previous subsection, the BAO/non-BAO ratio when varying  $\Delta Z_{\text{Max}}$  and the number of spectroscopic redshift bins. The no-BAO forecast is estimated by using the Eisenstein-Hu power spectrum without the BAO wiggles. In paper-I we showed that the cross-correlations between narrow and close redshift bins has a higher (radial) BAO contribution compared with the auto-correlations. This is reflected in dark energy constraints depending stronger on BAO when these (radial) cross-correlations are included.

Subsection 3.6 include the four main forecast tabulars (Table 4,5), each corresponding to a different FoM. The different rows corresponds to probes, defined by which galaxy populations (photometric, spectroscopic) included, if the surveys overlap observable (counts, shear) are used and if some cross-correlations are removed. Columns correspond to modifying some effect, as removing WL, magnification, RSD or BAO and if marginalising or fixing the galaxy bias. For the combined overlapping photometric and spectroscopic survey, the bias is the physical effect with largest impact on the  $\gamma, w_0, w_a$  combined figure of merit  $\text{FoM}_{w\gamma}$ . When marginalising over the bias (free bias), the next effect

in relative importance is WL (factor of 4.8), RSD (factor 2.1), BAO (factor 1.3) and magnification (1%). Magnification is discussed separately in subsection 3.7, comparing with the literature and clarifying the difference in notation with Gaztañaga et al. (2012).

Two photometric (F) and spectroscopic (B) surveys increase  $\text{FoM}_{w\gamma}$  equivalent to 30% larger area when overlapping. The benefit is smaller for a known galaxy bias. Overlapping surveys (FxB) improve the constraints for two reasons. Additional cross-correlations for overlapping surveys can explain part of the gain. One can cross-correlate the F and B galaxy counts, and also foreground spectroscopic counts with the shear from the photometric survey. The second contribution is the additional covariance since the overlapping surveys (F and B) trace the same matter fluctuation. This advantage of two galaxy population has already been show in 3D  $P(k)$  (McDonald & Seljak 2009) and 2D correlations (Asorey, Crocce & Gaztañaga 2014). Here we extend those findings to WL and RSD for the combination of the F and B samples. Eriksen & Gaztanaga (2014a) explain these effects in more detailed and compares our forecast to other analysis in the literature.

## ACKNOWLEDGMENTS

We would like to thank the group within the DESI community looking at overlapping surveys. M.E. wish to thank Ofer Lahav, Henk Hoekstra and Martin Crocce in his thesis examination panel, where these results were discussed. E.G would like to thank Pat McDonald for exploring and comparing results. Funding for this project was partially provided by the Spanish Ministerio de Ciencia e Innovacion (MICINN), project AYA2009-13936 and AYA2012-39559, Consolider-Ingenio CSD2007- 00060, European Commission Marie Curie Initial Training Network CosmoComp (PITNGA-2009-238356) and research project 2009- SGR-1398 from Generalitat de Catalunya. M.E. was supported by a FI grant from Generalitat de Catalunya. M.E. also acknowledge support from the European Research Council under FP7 grant number 279396.

## APPENDIX A: IMPACT OF NON-LINEAR SCALES

The fiducial forecast include Halofit-II, use  $10 \leq l \leq 300$  and remove correlations entering into non-linear scales (subsection 2.2). To test the impact of non-linear scales, Fig.A1 show the  $\text{FoM}_{w\gamma}$  ratio between including non-linear  $P(k)$  (Halofit II) and only the corresponding linear spectrum (from Eisenstein & Hu 2003, EH). On the x-axis is the maximum multipole included,  $l_{\text{max}}$ , which fiducially is  $l_{\text{max}} = 300$ . The top panel shows this ratio using all correlations until the  $l_{\text{max}}$  cut. As expected, the ratio increase with  $l_{\text{max}}$  and it is largest when only including galaxy counts.

The bottom panel illustrate the effect of an additional cut to remove correlations entering into non-linear scales  $k > k_{\text{max}}$ . For  $l_{\text{max}} = 300$  the  $\text{FoM}_{w\gamma}$  including Halofit is for FxB:Counts respectively 30% and 80% higher than EH only when removing or using all correlations. With increasing  $l_{\text{max}}$ , the ratio with "All" correlations grows quite

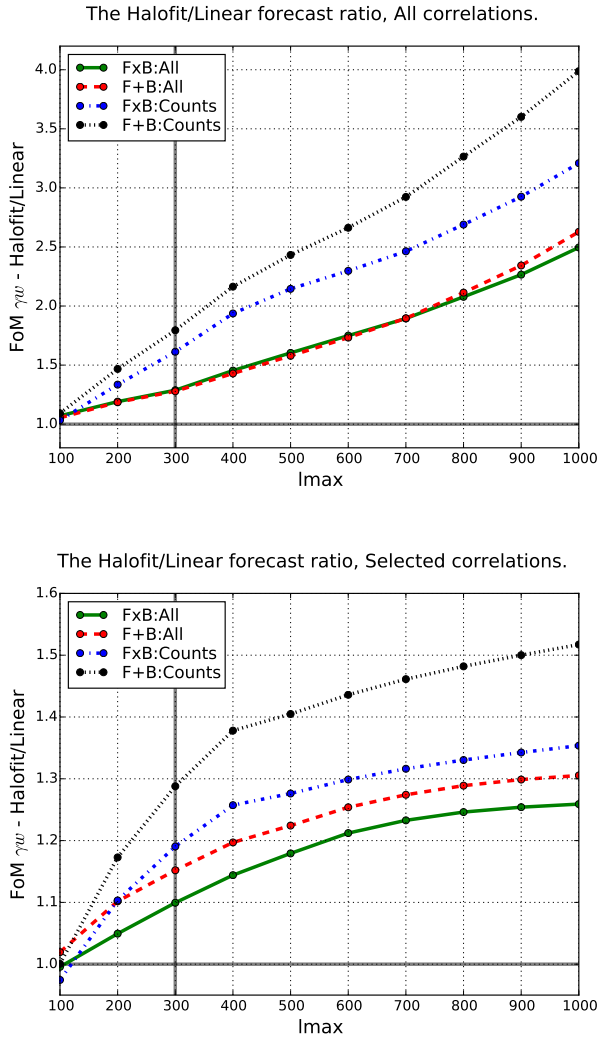


**Figure A1.** Forecast ratio between including the Halofit contributions or only the linear (Eisenstein-Hu 2003) power spectrum. The figure of merit is  $\text{FoM}_{w\gamma}$  and the lines corresponds to FxB:All, F+B:All, FxB:Counts and F+B:Counts. In the top/bottom panel, the ratios include/exclude correlations entering into non-linear scales ( $k > k_{max}$ ). A vertical line at  $l_{max} = 300$  mark the fiducial value.

linearly, while for the "selected correlations" the ratios flattens. The  $\text{FoM}_{\text{DETF}}$  and  $\text{FoM}_{\gamma}$  (not shown) follow the same pattern, but with smaller ratios. For  $\text{FoM}_w$  (not shown) the ratios are even flatter at high  $l_{max}$  and none of the probes cross the line 1.2. The fiducial forecast include Halofit, but we limit the correlations included to not become too sensitive to assumptions on the non-linear scales. In addition to the non-linear matter power spectrum, these scales could require a scale dependent galaxy bias. Note that these results are on the forecasted accuracy, which mainly depend on the observable derivative with respect to cosmology. The cut in non-linear scales for not biasing a parameter fit (precision) can be different and is not considered here.

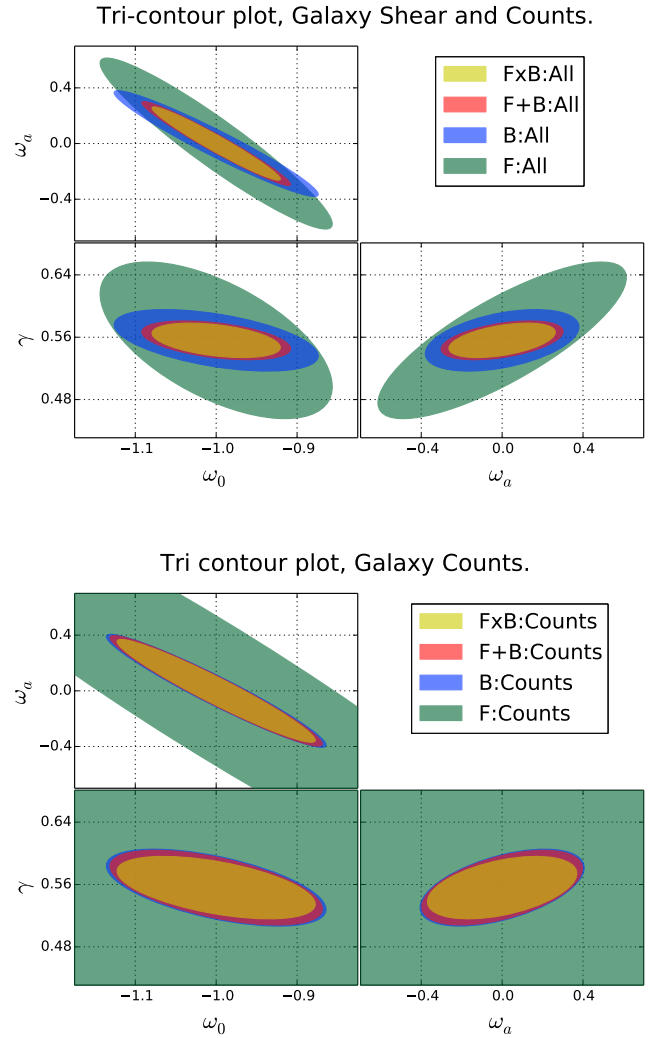


**Figure B1.** Contour plots of  $w_0$ ,  $w_a$  and  $\gamma$ . The three subplots show the Fisher matrix  $1-\sigma$  contours, marginalizing over the DETF parameters and galaxy bias. The top panel show contours for FxB:All, F+B:All, B:All and F:All, while the bottom panel only include galaxy counts.

## APPENDIX B: CONTOURS

Fig. B1 shows the  $1-\sigma$  contours for  $w_0$ ,  $w_a$  and  $\gamma$ . The top panel show for "All" and the combination FxB, F+B, F and B. One can see some trends also present in the tables. The combination F+B:All, combining shear and galaxy counts from separate surveys, is more powerful than analyzing the survey separately. The factor of 1.5 improvement of FxB:All over F+B:All corresponds to the difference between the two inner ellipses. On the bottom is a similar plot for the galaxy counts. Using equal scales allow us to directly compare the constraints, but at the expense of the F:Counts contours being plotted beyond the borders. For the galaxy counts the Bright population completely dominates, even if the Bright sample includes more bias parameters.

Last Fig. B2 looks at the effect of removing WL and RSD. The equivalent Magnification and BAO plots are not included since those effects are weaker, which results in less difference between the ellipses. The top panel shows FxB:All

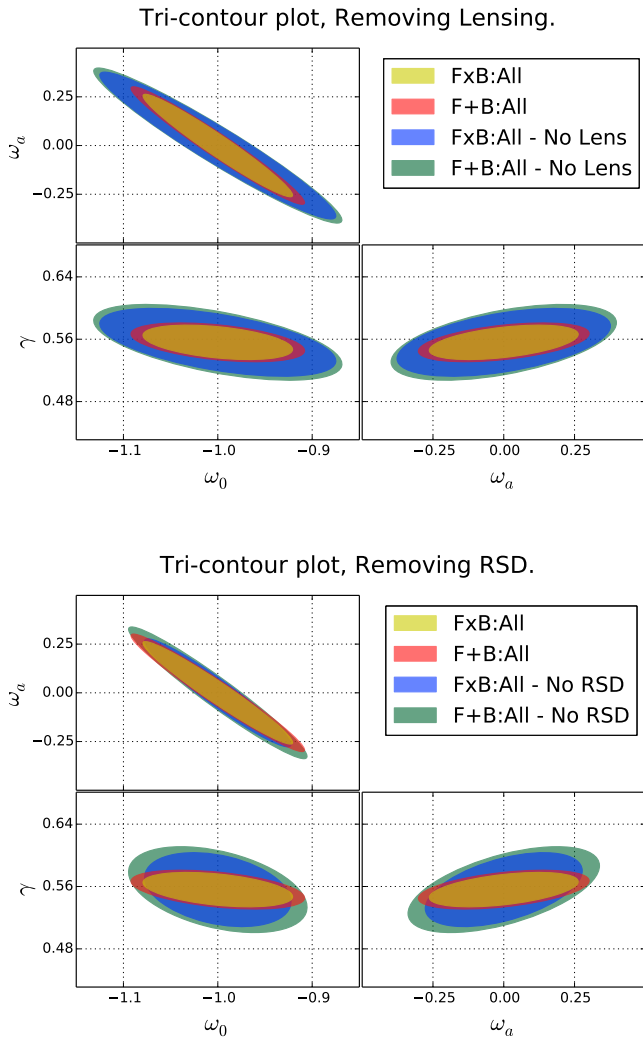


**Figure B2.** Contour plots of  $w_0$ ,  $w_a$  and  $\gamma$ . The three subplots show the Fisher matrix  $1\text{-}\sigma$  contours, marginalizing over the DETF parameters and galaxy bias. In the upper plot, two ellipses are the fiducial FxB:All and F+B:All, while two remove Weak Lensing observables. The bottom plot similarly show the fiducial FxB:All and F+B:All, and then two contours in real space.

and F+B:All in a tri-contour plot, with and without WL (fiducial and "No Lens"). The Weak Lensing improve the constraints on all three parameters included in the contour plots. Comparing the FoMs in Table 4 and 5, one see same-sky benefit of FxB:All is actually higher when including lensing.

In the lower panel is similar plot, instead with two contours calculated with and without RSD (fiducial and "No RSD"). While the RSD impact the parameter constraints different, the margins are exactly equal so one can visually compare the effects. The RSD is contributing strongly to measuring  $\gamma$  and less to  $w_0$  and  $w_a$ . One also see the same trend in the Tables 4 and 5. There the RSD improve  $\text{FoM}_{w\gamma}$ ,  $\text{FoM}_\gamma$  and  $\text{FoM}_w$  which depends on  $\gamma$ , while not  $\text{FoM}_{\text{DETF}}$  where  $\gamma$  is fixed. The difference between the contours in bottom panel show if RSD increases or decreases the importance of overlapping surveys. Including RSD, looking at the

numerical values in the table, slightly reduce the benefit of overlapping galaxy surveys.

## REFERENCES

- Albrecht A. et al., 2006, ArXiv e-prints, 0609591  
 Asorey J., Crocce M., Gaztañaga E., 2014, MNRAS, 445, 2825  
 Asorey J., Crocce M., Gaztañaga E., Lewis A., 2012, MNRAS, 427, 1891  
 Bardeen J. M., 1980, Phys. Rev. D, 22, 1882  
 Bernstein G. M., 2009, ApJ, 695, 652  
 Bernstein G. M., Cai Y.-C., 2011, MNRAS, 416, 3009  
 Bridle S., King L., 2007, New Journal of Physics, 9, 444  
 Cai Y.-C., Bernstein G., 2012, MNRAS, 422, 1045  
 Catelan P., Kamionkowski M., Blandford R. D., 2001, MNRAS, 320, L7  
 Crocce H. M., 2007, PhD thesis, New York University  
 de Putter R., Doré O., Takada M., 2013, ArXiv e-prints, 1308.6070  
 Di Dio E., Montanari F., Lesgourgues J., Durrer R., 2013, ArXiv e-prints  
 Dodelson S., 2003, Modern cosmology  
 Duncan C. A. J., Joachimi B., Heavens A. F., Heymans C., Hildebrandt H., 2014, MNRAS, 437, 2471  
 Dvali G., Gabadadze G., Porrati M., 2000, Physics Letters B, 485, 208  
 Efstathiou G., Bernstein G., Tyson J. A., Katz N., Guhathakurta P., 1991, ApJ, 380, L47  
 Eisenstein D. J., Hu W., 1998, ApJ, 496, 605  
 Eriksen M., Gaztanaga E., 2014a, (same-sky paper) ArXiv e-prints, 1412.8429  
 Eriksen M., Gaztanaga E., 2014b, (paper-I) ArXiv e-prints, 1412.2208  
 Eriksen M., Gaztanaga E., 2015, (paper III) In preparation  
 Font-Ribera A., McDonald P., Mostek N., Reid B. A., Seo H.-J., Slosar A., 2013, ArXiv e-prints, 1308.4164  
 Fry J. N., Gaztanaga E., 1993, ApJ, 413, 447  
 Gaztañaga E., Cabré A., Hui L., 2009, MNRAS, 399, 1663  
 Gaztañaga E., Eriksen M., Crocce M., Castander F. J., Fosalba P., Marti P., Miquel R., Cabré A., 2012, MNRAS, 422, 2904  
 Heath D. J., 1977, MNRAS, 179, 351  
 Heitmann K., Higdon D., White M., Habib S., Williams B. J., Lawrence E., Wagner C., 2009, ApJ, 705, 156  
 Heitmann K., White M., Wagner C., Habib S., Higdon D., 2010, ApJ, 715, 104  
 Hirata C. M., Seljak U., 2004, Phys. Rev. D, 70, 063526  
 Joachimi B., Bridle S. L., 2010, A&A, 523, A1  
 Kirk D., Lahav O., Bridle S., Jouvel S., Abdalla F. B., Frieman J. A., 2013, ArXiv e-prints, 1307.8062  
 Lawrence E., Heitmann K., White M., Higdon D., Wagner C., Habib S., Williams B., 2010, ApJ, 713, 1322  
 Linder E. V., 2003, Physical Review Letters, 90, 091301  
 Linder E. V., 2005, Phys. Rev. D, 72, 043529  
 Martí P., Miquel R., Castander F. J., Gaztañaga E., Eriksen M., Sánchez C., 2014, MNRAS, 442, 92  
 Massey R., Rhodes J., Leauthaud A., Capak P., Ellis R., Koekemoer A. e., 2007, ApJS, 172, 239  
 Matthews D. J., Newman J. A., 2010, ApJ, 721, 456

- McDonald P., Seljak U., 2009, *J. Cosmology Astropart. Phys.*, 10, 7
- Ménard B., Scranton R., Fukugita M., Richards G., 2010, *MNRAS*, 405, 1025
- Newman J. A., 2008, *ApJ*, 684, 88
- Peebles P. J. E., 1980, *The large-scale structure of the universe*
- Reid B. A. et al., 2012, *MNRAS*, 426, 2719
- Schrabback T. et al., 2010, *A&A*, 516, A63
- Scoccimarro R., Sheth R. K., Hui L., Jain B., 2001, *ApJ*, 546, 20
- Scranton R. et al., 2005, *ApJ*, 633, 589
- Seo H.-J., Eisenstein D. J., 2003, *ApJ*, 598, 720
- Seo H.-J., Eisenstein D. J., 2007, *ApJ*, 665, 14
- Shoji M., Jeong D., Komatsu E., 2009, *ApJ*, 693, 1404
- Springel V., 2005, *MNRAS*, 364, 1105